Montanuniversität Leoben

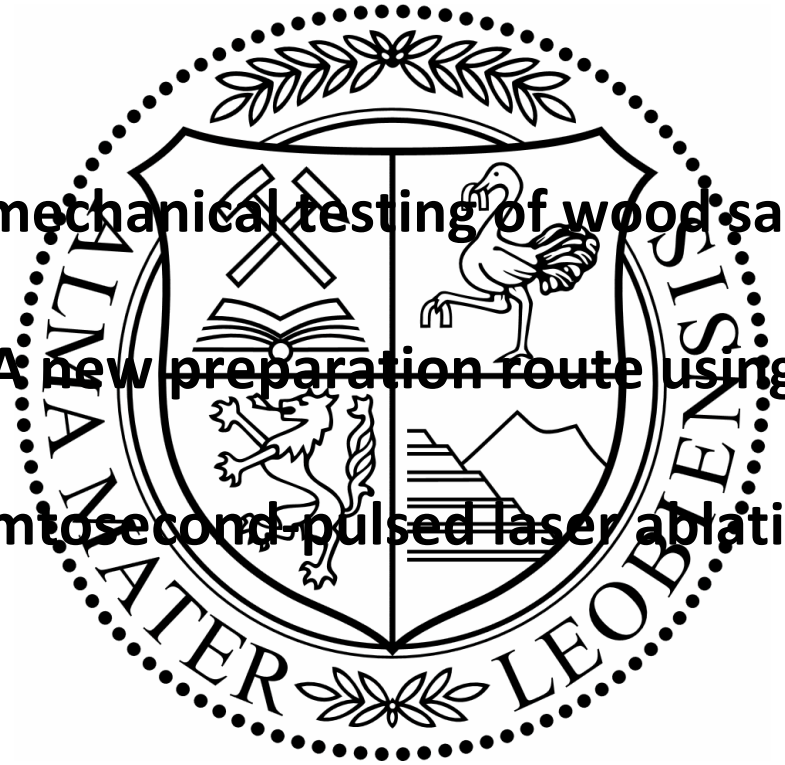

Micromechanical testing of wood samples: A new preparation route using femtosecond-pulsed laser ablation

Severin Jakob

Master thesis

Department of Materials Physics, Montanuniversität Leoben and

Erich Schmid Institute of Materials Science, Austrian Academy of Sciences

Affidavit

I declare in lieu of oath, that I wrote this thesis and performed the associated research myself, using only literature cited in this volume.

Eidesstattliche Erklärung

Ich erkläre an Eides statt, dass ich diese Arbeit selbstständig verfasst, andere als die angegebenen Quellen und Hilfsmittel nicht benutzt und mich auch sonst keiner unerlaubten Hilfsmittel bedient habe.

Date Signature

Micromechanical testing of wood samples: A new preparation route using femtosecond-pulsed laser ablation

Ultrashort-pulsed laser ablation becomes more and more important for micromachining. Any type of material can be processed with little or no damage to the surrounding volume due to the ultrashort pulse duration. In contrast to the Focused Ion Beam workstation laser ablation provides 4-6 orders of magnitude higher ablation rates and avoids ion implantation. In this work a solid-state laser with a wavelength of 515 nm and pulse duration of 318 femto-seconds (fs) was used to prepare wood samples from spruce for mechanical testing at the micrometre level. After optimisation of the different laser parameters, tensile and compressive specimens were manufactured from microtomed cross and tangential sections. For comparison a different preparation route, using an ion milling system and a copper mask, was used. Additionally, two laser-processed samples were exposed to an electron beam prior testing to study a possible beam damage. The specimens originating from these different preparation conditions were tested on a fibre tensile testing module and monitored with a stereo light microscope. Advantages and limitations of the fs-laser preparation technique, as well as the deformation and fracture behaviour of the samples, are discussed. The results have shown that fs-laser processing is a fast and precise preparation technique, which enables the production of samples with sizes at the microscale. Mechanical evaluation of tested tensile samples yielded comparable results to literature. Compression samples showed typical behaviour of cellular materials.

Mikromechanische Versuche an Holz: Eine neue Herstellungsmethode durch Einsatz von ultrakurz gepulster Laserablation

Laserablation mit ultrakurzen Pulsen ist eine aufstrebende neue Technologie zur Bearbeitung im Mikrometer-Bereich. Durch die ultrakurze Pulsdauer kann jedes Material ohne Beeinflussung der Randzone abgetragen werden. Laserablation hat dabei eine 4-6 Größenordnungen höhere Abtragsrate als die Bearbeitung mit einem Ionenstrahl. In dieser Arbeit wurde ein Festkörperlaser mit einer Wellenlänge von 515 nm und einer Pulsdauer von 318 Femtosekunden (fs) eingesetzt, um Fichtenholzproben für mikromechanische Versuche zu erzeugen. Es wurden die optimalen Einstellungen des Lasers für die Holzbearbeitung ermittelt und anschließend Zug- und Druckproben an Mikrotom-Dünnschnitten in Quer- und Längsrichtung hergestellt. Zum Vergleich wurden Proben mittels Ionen-Polierer und einer Kupfermaske angefertigt. Zwei durch den fs-Laser hergestellten Proben wurden einem Elektronenstrahl ausgesetzt, um dessen Einfluss zu untersuchen. Alle Proben wurden an einem Faserzugmodul getestet und gleichzeitig unter einem Stereomikroskop beobachtet. Vorteile und Einschränkungen bezüglich der fs-Laser Herstellung sowie Verformungs- und Bruchverhalten der getesteten Proben werden diskutiert. Die Ergebnisse zeigen, dass der fs-Laser eine schnelle und präzise Präparation von Proben mit Abmessungen im Mikrometerbereich ermöglicht. Zugfestigkeiten der getesteten Proben sind vergleichbar mit Literaturwerten. Druckproben zeigen das typische Verhalten von zellulären Materialien.

Acknowledgements

First of all, I would like to thank my supervisor Univ. Prof. Dr. Reinhard Pippan, Vice director of the Erich Schmid Institute of Materials Science of the Austrian Academy of Sciences for his support and trust in me doing this thesis.

Furthermore, I wish to thank Dipl.-Ing. Manuel Pfeifenberger, doctoral candidate at the Erich Schmid Institute, for his support regarding laser processing and lots of discussions. It was fun working together.

I gratefully acknowledge Sabine Herzele, MSc, from the Institute of Wood Technology and Renewable Materials of the University of Natural Resources and Life Sciences, Vienna for showing me the institute and preparing the thin sections.

Grateful acknowledgements go to Dr. Anton Hohenwarter for his assistance during the experiments and finalization of the thesis. Furthermore, I thank Dipl.-Ing. Alexander Leitner and Dipl.-Ing. Ruth Konetschnik for their help regarding nanoindentation and the masking technique and Franz Hubner for his support in the workshop.

Last but not least I would like to thank my family and friends for their ongoing support.

Content

1. Introduction 1
1.1. Wood: Structure and characteristics 2
1.1.1. Growth and macroscopic structure 2
1.1.2. Cellular structure of wood 3
1.1.3. Microstructure and chemical composition 5
1.2. Laser ablation 7
1.2.1. Laser fundamentals 7
1.2.2. Laser-matter interaction 9
1.2.3. Laser ablation of wood 10
2. Methods 11
2.1. Thin sectioning with a microtome 11
2.2. Laser ablation at the Erich Schmid Institute 12
2.3. Alternative processing with an argon ion polisher 14
2.4. Pillar compression 15
2.5. Fibre tensile module 16
3. Experimental 18
3.1. Sample preparation 18
3.1.1. From a tree to a thin section 18
3.1.2. Drying of specimens 19
3.1.3. Mounting for laser ablation 20
3.2. Optimization of laser parameters 21
3.2.1. Power 22
3.2.2. Divisor 23
3.2.3. Number of passes 25
3.2.4. Working distance 25
3.3. Cutting of pillars 27
3.4. Tensile specimens 27
3.4.1. Processing with ultrashort laser pulses 27
3.4.2. Tensile specimens produced by ion milling 29
3.4.3. Performing tensile tests 30
3.5. Compression samples for the fibre module 31
3.5.1. Laser processing 31
3.5.2. Compression tests with the fibre module 32

4. Results and discussion 33
4.1. Failure mechanism in tension described in literature 33
4.2. Observed failure mechanism in tension 34
4.2.1. Loading in longitudinal direction 34
4.2.2. Loading in radial and tangential direction 36
4.3. Quantitative analysis of tensile tests 39
4.3.1. Error estimation 39
4.3.2. Tensile strength 40
4.3.3. Elongation 41
4.4. Beam damage 41
4.5. Comparison of fs-laser processing and ion milling 43
4.5.1. Surface quality 43
4.5.2. Mechanical behaviour 45
4.6. Compressive specimens 45
4.6.1. Pillar compression with the nanoindenter 45
4.6.2. Compression experiments with the fibre module 47
5. Summary 51
List of symbols and abbreviations 53
List of figures 54
List of tables 57
References 58

1. Introduction

For most materials there is an inverse relationship between desired properties. When one property is high, the other is low, e.g. strength and ductility or hardness and fracture toughness. One aim of material science is to gain improvements in both of these normally exclusive properties or at least an increase in one property with little or no impairment to the other. Advances in this regard provide possibilities for new structural materials and technologies. Biological materials, however, seem not to be subject to this restriction, because of their use of different materials and complex structure in one compound. For example, Nacre is a compound of platelets of aragonite, which is a ceramic, separated by a matrix of organic polymers. This arrangement of hard and brittle platelets in a soft, ductile matrix provides both, high hardness and high fracture toughness. The optimal performance of the material strongly depends on the dimensions of the structures. Another example for combining strength and light-weight design is wood. To understand the mechanics behind the hierarchical structure of wood, one needs to know the properties on every length scale. There is still a lot of progress needed to generate and implement bioinspired materials into technical applications [1].

There have been a lot of attempts to characterize the mechanical properties of wood on the micrometre scale. A recent review has been published by Eder et al. [2]. In general, a lot of effort has to be put into getting mechanical values. With small sample sizes it is hard to measure mechanical properties directly. Another problem with every biological material is that there is a strong influence of the water content. In most cases the wood samples are dried during the preparation, especially if they have to be handled in vacuum. This has an effect on the mechanical properties, even after increasing the water content again for testing [3]. Nevertheless, it can be assumed that samples tested in vacuum are completely dry. In-situ tests in a scanning electron microscope (SEM) and ex-situ tensile tests have been performed on single wood fibres after mechanical isolation to gain stress strain curves. To calculate the stress from measured forces, one way is to measure the ruptured surface after the test. For strain measurement video extensometry and digital image correlation have been used [4–6]. The focused ion beam workstation (FIB) has already been used to prepare samples in the micrometre range. Orso et al. used the FIB and a micromanipulator to determine the bending modulus of a spruce wood cell wall [7]. In other experiments the FIB was used to prepare pillars out of the cell wall and the middle lamella for uniaxial compressive testing [8–10]. Another method to determine hardness and elastic modulus at this length scale is nanoindentation. Here mostly a three- or four-sided pyramid is pressed into the material and force and displacement are measured [11, 12]. Jäger et al. calculated the longitudinal stiffness and the traverse and shear modulus from nanoindentation measurements [13].

Ultrashort pulsed laser ablation becomes more and more important for micromachining. The removal of material in the length range of micrometres provides many possibilities for

manufacturing small-scale structures for example in microelectronics or biomedicine. The most important tool till now is the FIB. Here ions are accelerated towards the sample and sputter material off the surface. In contrast to the FIB, laser ablation provides higher ablation rates and avoids ion implantation [14]. The latter is an inherent mostly negative feature of the FIB. The ion bombardment leads to defects and changes in the chemical composition at the surface of the sample [15]. Laser ablation, however, provides such a high energy density that the illuminated volume is removed regardless of the type of material. Because of the ultrashort pulse length, no heat transfer and therefore damage to the remaining material take place [16, 17].

The aim of this work is to evaluate the possibilities of femtosecond (fs) laser ablation as a new method to produce micrometre-sized wood samples for mechanical testing.

1.1. Wood: Structure and characteristics

Trees evolved around 370 million years ago. Because of the competition for sunlight, these plants developed wooden stems to support their branches and leaves high above the ground. Some species can grow over 100 m. The wooden stem provides not only support, but also transports water and mineral solutions. Wood is a cellular material and has a hierarchical structure leading to a high specific strength and an optimized resistance against buckling.

Wood has been used since early human history. Applications include tools, weapons or fire wood, later on also furniture and musical instruments. Wood has been and still is used in construction for housing and architecture.

1.1.1. Growth and macroscopic structure

The trunk of a tree has different functions. First it must provide the mechanical support for the crown including leaves, fruits and seeds. Second it must transport water and minerals to the leaves, where photosynthesis takes place. Lastly the products of photosynthesis are transported and stored. [18]

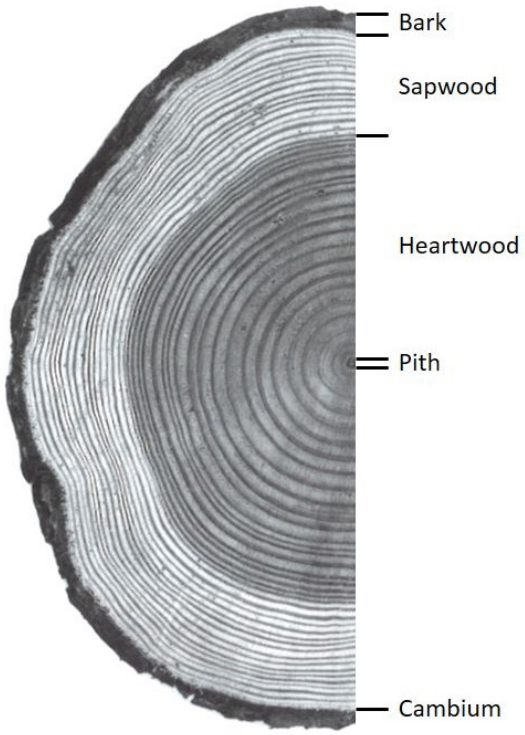

Fig. 1. Cross section through a fir tree (adapted from Dinwoodie, 2000) [18]

Fig. 1 shows the cross section of a fir tree. In the middle of the cross section is the so-called pith. Next to it is the heartwood. It used to transport water and minerals when the tree was younger. Now it has no other function than mechanical support. It has higher acidity to protect the wood against insects and fungi and often is a different colour than the subsequent sapwood. The sapwood can make up 10 to 60 % of the trunk, depending on species, age and growth conditions. Besides also providing mechanical support, the cells in the sapwood transport water, minerals and carbohydrates. Next to the sapwood is the so-called cambium. This is where the tree actually grows. In season-like climates like in Austria trees show a characteristic growth behaviour. During spring a lot of water and minerals are needed to grow new leaves. Therefore, the tree forms cells with large cross sections and thin cell walls. In summer and autumn, the tree forms cells with thicker walls to provide stronger mechanical support for the coming winter. This leads to the forming of distinctive rings, so called annual or growth rings. Since this phenomenon repeats itself every year, the age of a tree can be determined after cutting by counting the annual rings in the cross section. The outermost layer is the bark, which has mainly a protective function. [18]

1.1.2. Cellular structure of wood

The cellular structure of wood is different for soft- and hardwoods. Softwoods are for example pine or spruce. They have two main cell types, which are tracheids and parenchyma cells.

Tracheids represent up to 95 % of the mass and are responsible for mechanical support and water transport. The parenchyma cells have a storage function. Hardwoods, for example oak or beech, are evolutionary younger than softwoods and therefore have a more diversified cell structure. They have tracheid and parenchyma cells as well, but also fibres solely for mechanical support and vessels for conduction. Most cells are aligned in the longitudinal axis of the stem, but some are aligned in radial direction. These groups of cells are called wood rays. [18]

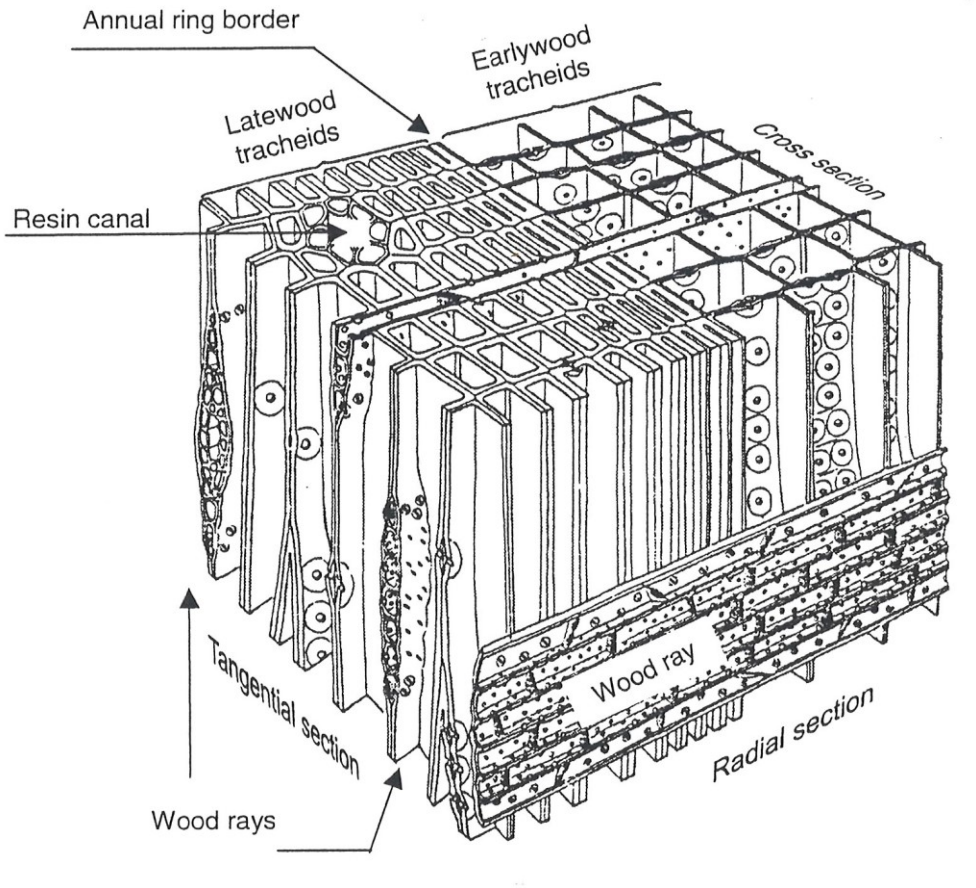

Fig. 2. Three-dimensional model of softwood structure (adaptation from Mägdefrau, 1951) [19]

Fig. 2 shows the softwood structure, consisting mostly of tracheid cells, further distinguished into earlywood and latewood tracheids. These cells are formed like hollow tubes aligned parallel to the longitudinal axis of the stem. The earlywood tracheids are formed in spring and have a large hollow cross section, called lumen, for fast transport of water. The cell walls of earlywood cells are thin. The latewood tracheids are formed in summer and autumn and have thicker cell walls for mechanical support. Typical dimensions of these cells are 20 to 30 micrometres in cross section with 2 to 7 micrometres wall thickness and about 2 to 3 millimetres in length. To enable transport across more than one tracheid cell, the cells are

connected via so-called pits. These are holes in the cell wall functioning like a valve. The parenchyma cells are mostly located in the wood rays and are responsible for storage. [19]

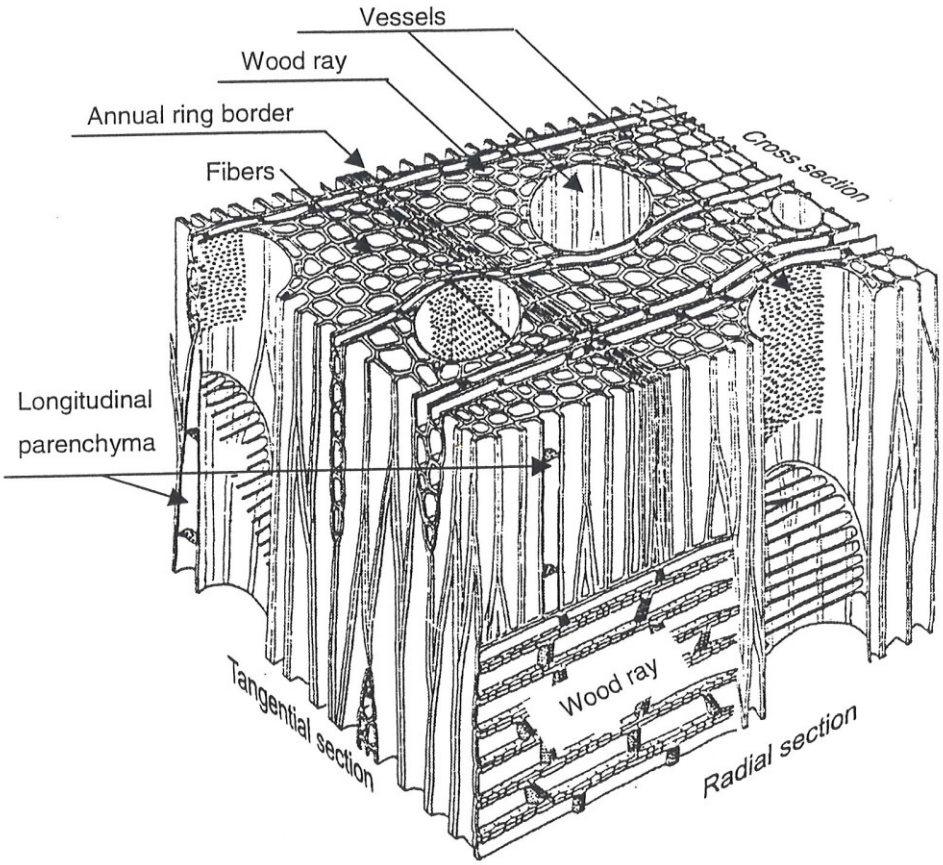

Fig. 3. Three-dimensional model of hardwood structure (adaptation from Mägdefrau, 1951) [19]

Fig. 3 shows a model of a hardwood structure. As already mentioned, hardwoods consist of a more complex cell structure. The fibre cells are similar in appearance to the tracheids but have no transport function. They have thick cell walls for mechanical support. The vessels in hardwood take on the transport function. Their diameter ranges from 50 to 500 micrometres and they can be several metres long. There are more parenchyma cells, which also lie in longitudinal direction, than in softwoods. [19]

1.1.3. Microstructure and chemical composition

Wood consists of cellulose, hemicellulose, lignin and other extractives. Cellulose makes up 40 to 45 % of the mass of wood. It is a long chain of glucose monomers with a polymerization of 1000 to 10000 units. The cellulose chains are aligned in microfibrils which have crystalline

structure and are highly orientated. Hemicellulose, 25 to 30 % of the mass, is also composed of sugar monomers but not in a linear manner. Both crystallinity and polymerisation are low. Lignin constitutes 20 to 28 % of the mass with lower percentages in hardwoods. It is a complex aromatic molecule composed of phenyl groups. Extractives is a collective name for different organic compounds, like waxes, sugars and resins, mostly responsible for protection against insects and fungi. They account for up to 5 % of the mass. In principle cellulose constitutes the fibre and hemicellulose and lignin build up the matrix of the material. [18]

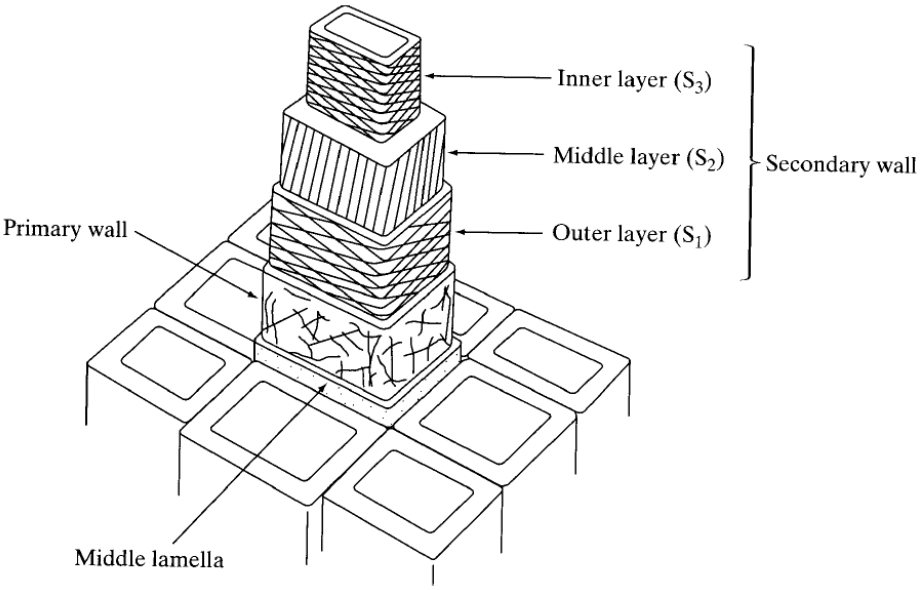

Fig. 4. Schematic structure of the cell wall of a softwood tracheid [18]

The principle structure of the cell wall for a softwood tracheid is shown in Fig. 4. The orientations of the cellulose microfibrils are indicated for the different cell wall layers. The primary wall consists of randomly orientated and loosely packed cellulose microfibrils. In the secondary cell wall the microfibrils are highly orientated and parallel to each other. The outer layer of the secondary wall, the so-called S_1 layer, consists of microfibrils aligned gradually from a left- to a right-hand spiral at angles from 50 to 70° to the longitudinal axis. The middle layer of the secondary cell wall (S_2) makes up most of the volume of the wood cell wall. It consists of parallel microfibrils aligned in a right-hand spiral at an angle of 0 to 30°, called the microfibril angle (MFA). Since S_2 is the most dominant layer, the mechanical behaviour depends strongly on the MFA. The inner layer of the secondary cell wall (S_3) has similarly orientated microfibrils as the S_1 layer with angles varying between 60 and 90°. The S_3 layer is thinner than the S_1 layer. Between adjacent cells is the middle lamella, which is a lignin-rich phase.

1.2. Laser ablation

Laser ablation and especially ultrafast laser processing has become an important field for fundamental research and also industrial applications. With its inherent features, such as high energy density and precision, laser ablation is used for micromachining in material research, microelectronics and biomedicine [20]. Any type of material can be processed with little or no damage to the surrounding volume due to the pulse duration in the range of femtoseconds [16]. The first experiments with ultrashort laser pulses were done with UV excimer lasers [21, 22]. Since then laser ablation has become a rapidly growing field with a wide range of processed materials and implementation into industrial applications [23, 24].

For more information on the topic, see for example 'Ultrafast laser processing', Pan Stanford Publishing, 2013 [17], or 'Lasers in Materials Science', Springer, 2014 [25].

1.2.1. Laser fundamentals

The term LASER originates from the acronym "Light Amplification by Stimulated Emission of Radiation". Through the stimulated emission of photons, a strong coherent light source with specific wavelength and narrow spectral width can be generated.

For the laser principle, a population inversion of electrons in a laser medium is needed. This means that more electrons are in the energetic-excited state than in their original ground state. The gain medium can be a solid, liquid, gas or plasma and provides the necessary energy states. The electrons have to be "pumped" into the excited state. This is mostly achieved by optical means. The excited states are metastable and therefore the electrons will randomly fall back to their original state after some time. In this process a photon is released with the energy corresponding to the energy difference between the two states. If a photon hits an excited electron, the electron jumps to its original state immediately and emits another photon with the same phase, frequency and direction. This process is called stimulated emission. The two photons are now coherent. The light is amplified in the gain medium between two mirrors, one of which is semi-transparent. There the amplified light beam can be partly extracted. [25]

Solid-state lasers use a solid gain medium, mostly an artificial crystal or ceramic doped with rare-earth atoms. Many different materials are used for modern solid-state lasers. One popular system in material science is Ti-doped sapphire as a gain medium because of its tuneable properties [26]. Different widely used materials are for example neodymium- or ytterbium-doped yttrium aluminium garnet (Nd:YAG, Yb:YAG). The doping atoms provide the needed energy bands for pumping the electrons into the excited state. In the case of Yb:YAG the absorption band lies at 940 nm and is 18 nm wide, which means that the electrons can be easily pumped by InGaAs laser diodes [27].

Especially for laser ablation high laser energy is needed. This is realized by pulsed operation. To get ultrashort pulses, mode locking is used. The distance between the two mirrors of a laser allows for a set of frequencies to form standing waves by interference. These are the longitudinal modes of the laser cavity. If these modes are phase locked, interference of the laser light results in bursts of energy. The reachable pulse duration or width is inversely proportional to the optical bandwidth of the pulse. This means that for shorter pulses the laser must provide a sufficiently broad bandwidth of light. Another restriction is that the average power is constant. Therefore, higher pulse powers can only be achieved by reducing the repetition rate. [25]

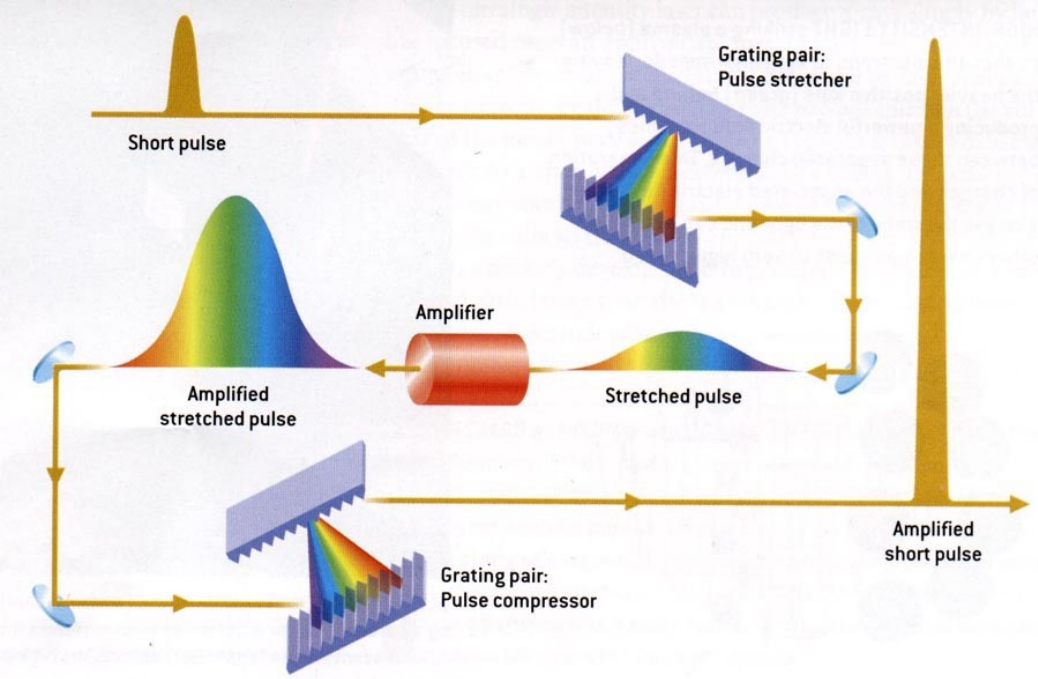

Fig. 5. Scheme of Chirped Pulse Amplification [25]

Another way to get high pulse energies is to amplify the initial pulse. Fig. 5 shows the schematic arrangement for the so-called Chirped Pulse Amplification. Amplifying the initial pulse directly would damage the optics. Therefore, the pulse is first stretched, meaning the bandwidth of the pulse is widened while simultaneously the peak intensity is lowered. Now the pulse can be amplified without damage to the optics. After that the pulse is compressed again to the original pulse duration, now having higher peak intensity. [17, 28]

1.2.2. Laser-matter interaction

Laser ablation takes place through absorption of laser energy. For short pulses (> 10 ps) this happens by heating the material in the focal region of the laser first to melting temperature and subsequently to vaporization temperature. The absorption mechanism of energy depends on the material. Transparent materials, for instance glass or certain plastics, cannot be ablated. The absorption mechanisms change for ultrashort pulses (< 10 ps). Because of the short interaction time and high laser intensities, absorption takes place through nonlinear processes [29].

For transparent or dielectric materials there are two processes responsible for the optical breakdown and ablation: first, avalanche ionization and second, multiphoton ionization. In avalanche ionization, free or conduction electrons, initially coming from impurities in a dielectric material, can absorb laser energy and gain kinetic energy. Then the first seed electron collides with a bound electron resulting in two free electrons. This repeats itself until enough electrons are ionized to form a plasma with critical density. Now the material becomes absorbing. If the laser field strength is even higher, which is the case for ultra-short pulses, bound electrons can be ionized directly through multiphoton absorption. This means that several photons provide the energy to move a bound electron to the free state contrary to the case of single-photon absorption (Fig. 6). [17, 29]

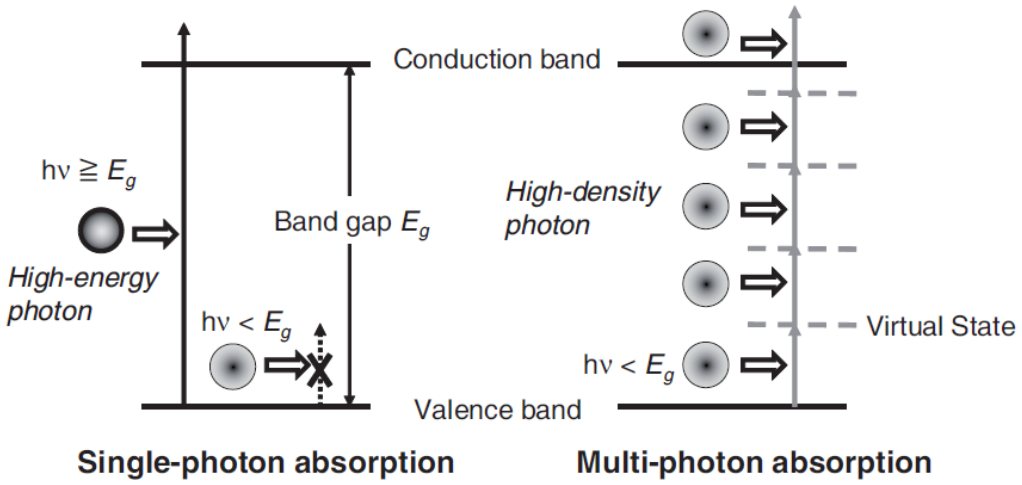

Fig. 6. Electron excitation by single- and multi-photon absorption [17]

In metals there are many free electrons available, which can absorb the laser energy. The ablation of material is then described by the Two-Temperature Model [30]. With small pulse widths, laser field strength is high and interaction time is short. The electrons, regardless if already free or first ionized, are heated to high temperatures, while the heavy ions remain relatively cold. Subsequent electron-ion energy transfer leads to vaporization of a large

fraction of the material. The amount of energy transfer depends on pulse duration and the energy coupling coefficient. [17]

The laser fluence is the energy density of the laser pulse. Every material has a certain fluence threshold before ablation takes place. Above this threshold the ablation depth is determined by the laser fluence. To estimate the fluence at a specific laser power, the pulse energy of one pulse is calculated according to equation (1).

$$E_{pulse} = \frac{P}{f} \qquad (1)$$

Here, E_{pulse} stands for the pulse energy and P for the average laser power at pulse repetition rate f. The fluence $E_{fluence}$ can be calculated according to equation (2) as the pulse energy over the focal area A_f of the laser spot.

$$E_{fluence} = \frac{E_{pulse}}{A_f} \qquad (2)$$

With ultra-short pulses almost all of the laser energy is used for ablation. The small portion of absorbed intensity is easily accommodated by heat conduction and dissipation. This means that no heat-affected zone at the edge of the remaining material is expected. [16, 17]

1.2.3. Laser ablation of wood

Laser machining on wood has already been used for marking and engraving [31]. Another major application is incising lumber for impregnation with adhesives and preservation agents [32]. For this purpose, CO_2-lasers with high power and long pulses are used because of their relatively low cost. Also, continuous wave (CW) lasers are used for cutting wood [33]. However, long pulses or CW lead to a large heat-affected zone with melting of the wood components and carbonization as shown in literature [34, 35]. As early as 1995, UV-laser irradiation is reported as a method to open the machined wood surface for glue or coating agents [36]. Recent experiments with a UV-laser and pulse duration of a few ns showed no change in texture of the wood although heat accumulation of the laser pulses can lead to carbonization [37]. Ultrafast laser processing of wood showed no carbonization of the remaining material and the ablation mechanism expected for dielectric materials [38, 39]. The processed surface has a one micrometre thick layer of spherical particles, which seem to have melted during and re-solidified after the laser pulse [40].

2. Methods

In this chapter a brief overview of the instruments and devices used for the conduction of the experiments is given. The sectioning of thin wood samples was done with a microtome at the Institute of Wood Technology and Renewable Materials of the University of Natural Resources and Life Sciences, Vienna. The laser system used for ablation is located at the Erich Schmid Institute of Materials Science in Leoben. The setup is explained and furthermore the devices for compressive and tensile tests are described.

2.1. Thin sectioning with a microtome

Thin sectioning with a microtome is a standard preparation technique for biological materials and polymers. The goal is to get thin sections for investigation with light or electron microscopes. Only hard materials can be processed, therefore soft materials have to be embedded or cut at sub-zero temperatures. In addition to the hardness, the knife geometry plays an important role for the quality of the sections (Fig. 7).

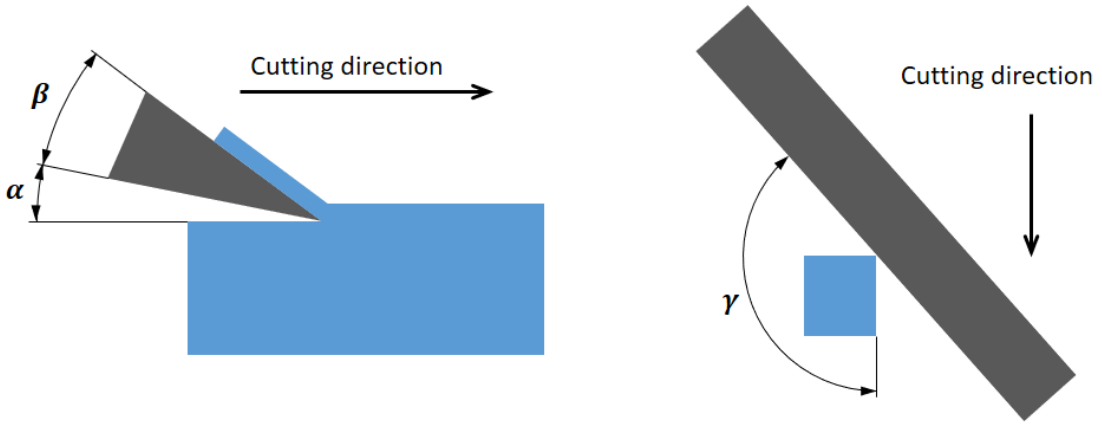

Fig. 7. Schematic knife geometry of a microtome; left: side view with clearance angle α and knife angle β, right: top view with declination angle γ

Several types of microtomes can be distinguished according to their cutting direction and environmental conditions. Sledge microtomes have a linear cutting direction. Either the sample is moved relative to a fixed knife or vice-versa. A defined cutting depth is necessary to gain reproducible thicknesses. The knife can be aligned with a declination angle regarding the moving direction to enable a smoother operation (see Fig. 7). Rotary microtomes use a rotating blade to cut thin sections off a sample. Typical thicknesses of sections cut by these types of microtomes are 30 to 500 µm. Vibrational microtomes can produce finer sections

because the vibrations lower the needed cutting force. A cryomicrotome has a chamber cooled with liquid nitrogen. At these low temperatures biological materials as well as polymers become hard and therefore thinner slices are possible. Ultramicrotomes allow the preparation of sections with thicknesses down to a few tens of nanometres. These sections are used for transmission electron microscopy. For more information on thin sectioning with microtomes see for example B. Bracegirdle: '*A history of microtechnique*', Heinemann Educational Books, 1978 [41].

2.2. Laser ablation at the Erich Schmid Institute

The laser system at the Erich Schmid Institute of Materials Science in Leoben is a modified ZEISS Auriga Laser, which is a combination of a dual beam SEM/FIB and a Onefive Origami XP ultrashort pulsed laser.

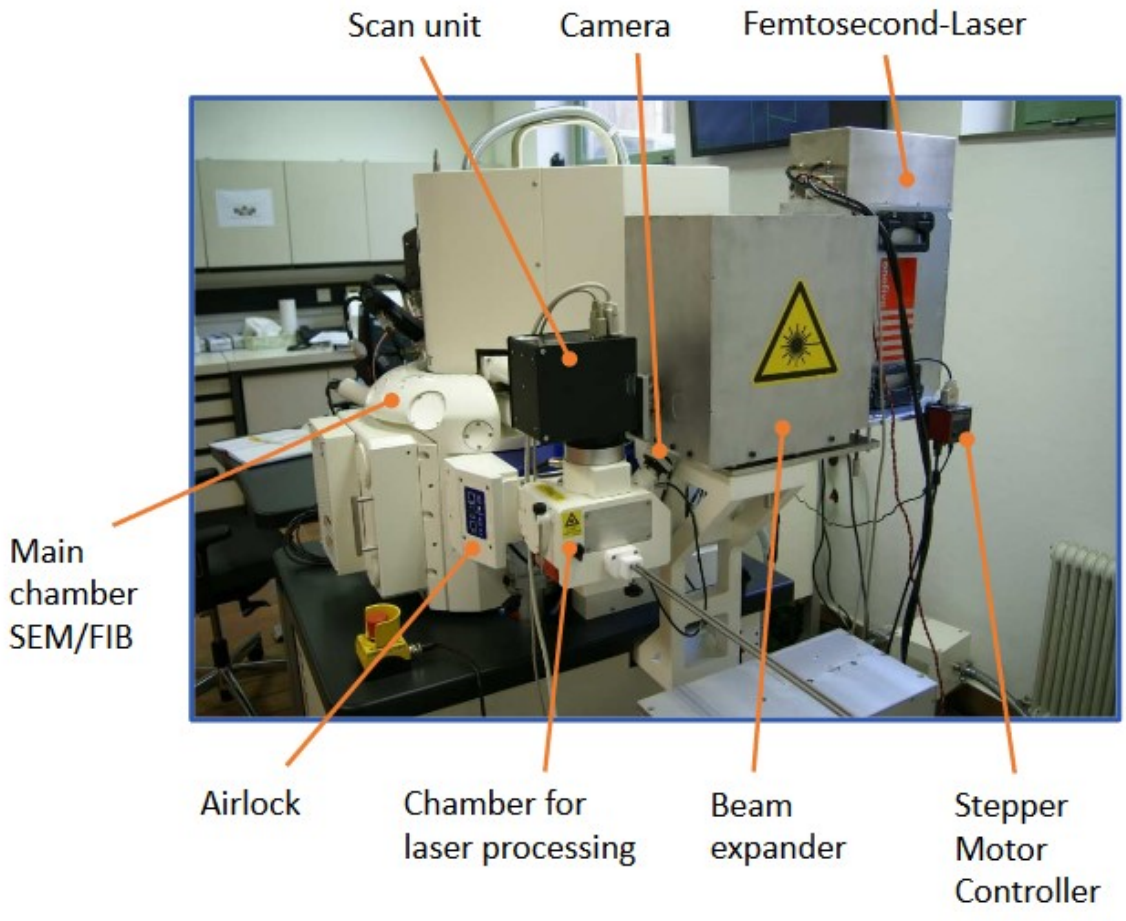

Fig. 8. Photograph of the laser system giving an overview with main components labelled (courtesy of M. Pfeifenberger, Erich Schmid Institute, 2016)

Fig. 8 gives an overview of the different components of the laser equipment. The laser pulses are generated by the laser unit at the back of the construction. The solid-state laser can operate at a 1030 or 515 nm wavelength with a maximum output power of 4 W and a maximum pulse repetition rate of 1 MHz. The pulse duration is 318 fs. With the beam expander, actuated by a stepper motor, the working distance (WD) in the laser chamber can be adjusted according to the sample height. The beam expander works in principle like an inverse Galileian telescope (Fig. 9). A dispersal lens widens the laser spot and the consecutive convex lens collimates the beam again. By changing the distance of the dispersal and the convex lens the WD in the laser chamber can be adjusted.

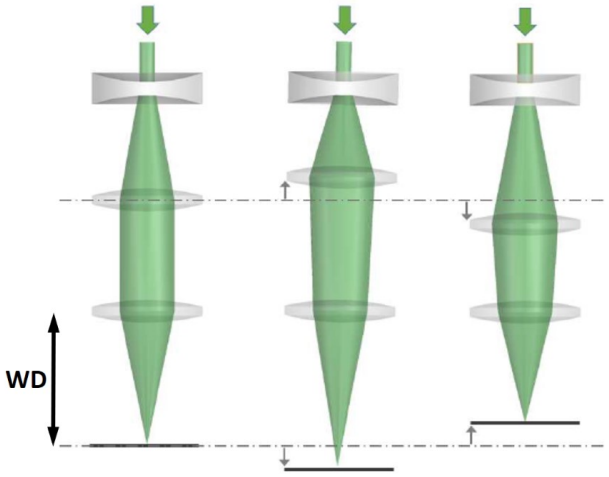

Fig. 9. Scheme of the beam expander for adjusting the WD (courtesy of M. Pfeifenberger, Erich Schmid Institute, 2016)

Within the scan unit two perpendicularly aligned mirrors (labelled 3 and 4 in Fig. 10) deflect the laser spot into the ablation chamber. The mirrors are actuated by galvanometers and can deflect the laser to a specific region. After the two mirrors an f-theta lens (5) focuses the laser to a diameter of about 30 µm on the sample surface. This results in a sufficiently high energy density for ablation. The f-theta lens system allows to focus the laser on a flat common plane within the laser chamber. A single convex lens would focus the laser on a curved image plane. The chamber for laser processing is pumped to a vacuum of 10^{-3} mbar and separated by an airlock from the main chamber. The laser chamber can be observed by a camera. Samples are inserted into the chamber for laser processing and can be transferred to the main chamber via a manipulator rod. In the main chamber SEM and FIB operations take place.

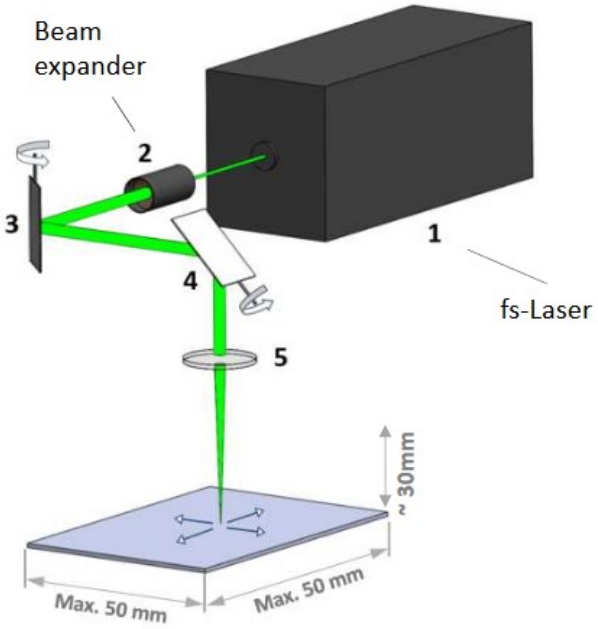

Fig. 10. Principle setup of the laser system (courtesy of M. Pfeifenberger, Erich Schmid Institute, 2016)

The complete setup allows machining of samples with fast laser ablation before moving the sample to the main chamber for a possible fine machining step with the FIB. Another possible application is polishing of sample surfaces with the laser for subsequent electron backscatter diffraction measurement [42]. The combination of SEM/FIB and laser ablation in one system provides fast processing and analysis without the need of transferring the sample between different devices. With the different chambers, separated by an airlock, contamination of the main chamber by laser machining can be avoided.

2.3. Alternative processing with an argon ion polisher

A different approach for the generation of micrometre-sized samples was the use of an ion milling system with a masking technique. In contrast to an FIB, this ion milling system uses Ar^+ ions instead of commonly used Ga^+ ions. Furthermore, the acceleration voltage is lower since it is normally used for polishing surfaces of cross sections. Both features reduce the energy input and therefore the possible beam damage.

The Hitachi High Technologies E-3500 ion milling system uses a three-electrode ion gun with the Penning system, where a magnet is incorporated to improve charging efficiency (Fig. 11). A plasma from the Ar gas flow is generated by applying a discharge voltage of 0 to 4 kV. The ions are accelerated through an aperture by the third electrode with 0 to 6 kV acceleration voltage.

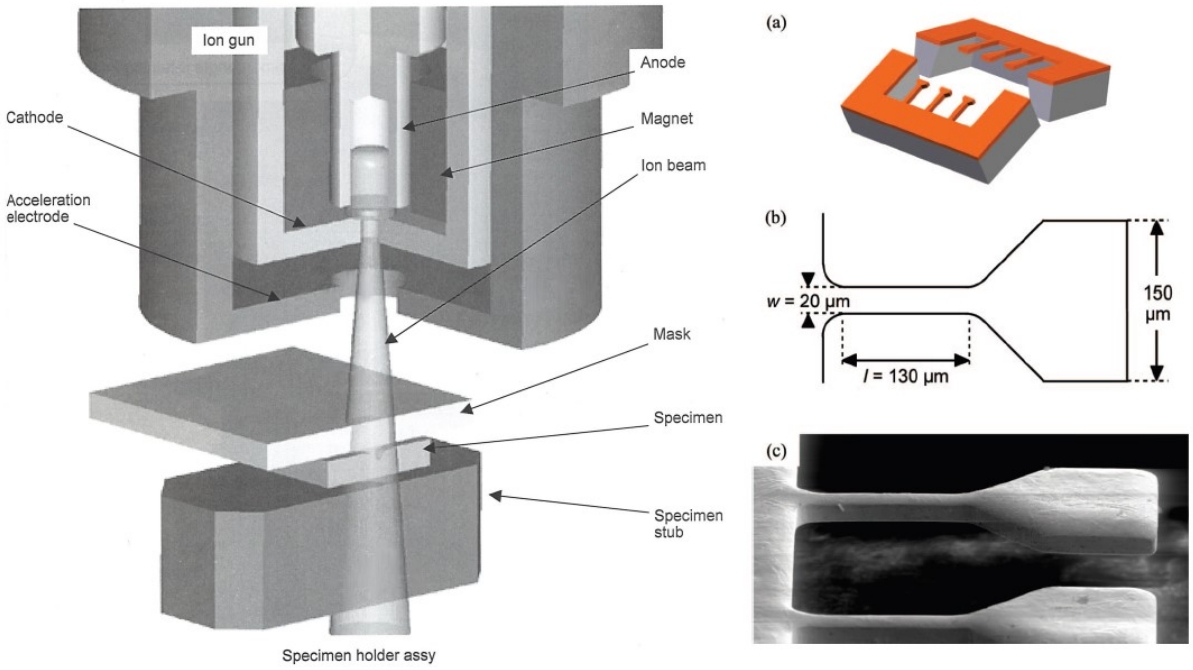

Fig. 11. Schematics of the ion gun and sample stage (left) and the free-standing copper specimen used as a mask (right) [43, 44]

In a former research project Smolka et al. performed in-situ tensile tests of free-standing copper samples, which can be seen in Fig. 11 [44]. The free-standing structures were produced by photolithography and etching with 30 % KOH on a silicon wafer. Since there was a variety of different dimensions of these samples available, the desired geometry was used as a mask.

2.4. Pillar compression

Pillar compression has become an intensively studied field since Uchic et al. showed that the mechanical properties depend on the sample size for micromechanical testing [45]. This method is a variation of widely used nanoindentation. In nanoindentation or instrumented indentation a so-called indenter, mostly a sharp three- or four-sided pyramid, is pressed into a material and force and displacement are measured with high precision. From the measured curve elastic modulus and hardness can be calculated [46, 47]. The hardness values cannot be transformed into a yield strength directly because of the complex stress and strain distribution under the tip. There are also other indenters like filaments or flat punch indenters available.

The basic step for pillar compression is to machine a free-standing round or square pillar into a bulk material. This is commonly done with an FIB. In the next step the pillar is compressed in the axial direction with a flat punch indenter. The flat surface should be larger than the pillar top surface to ensure a uniform force introduction. The compression can be performed in-situ or ex-situ. The deformation mechanisms as well as stress and strain can be studied.

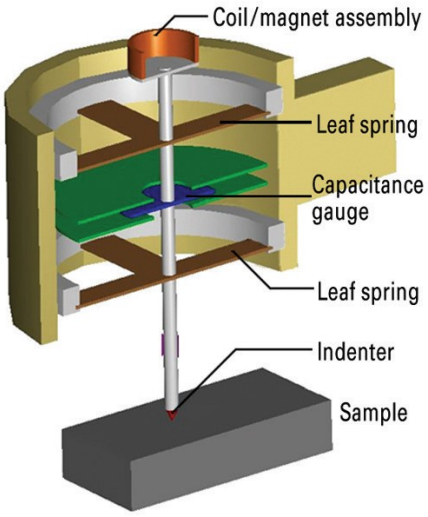

Fig. 12. Schematic diagram of the G200 Nano Indenter [48]

Pillar compression tests were conducted with a G200 Nano Indenter by Keysight Technologies [48]. The main components are indicated in Fig. 12. It has a capacitive displacement gauge with 0.01 nm resolution and 500 µm maximum displacement. A maximum load of 500 mN with 50 nN resolution can be applied by magnetic force. A conical diamond indenter with 40° angle and a flat tip with a diameter of 200 µm was used as flat punch indenter. The samples are mounted on an SEM sample holder on a special goniometer. The goniometer is used to align the sample perpendicular to the indenter. Before testing the indenter has to be calibrated with the microscope. For this purpose, a polished aluminium sample is used.

2.5. Fibre tensile module

For the measurement of micrometre-sized samples, a precise force and elongation detection is necessary. For this reason, a Kammrath & Weiß fibre tensile test setup was used [49]. The apparatus is able to measure forces up to 2 N with 10 µN resolution. The force measurement is done by frequency detection of an oscillating wire. Small changes of the load lead to a change in the resonance frequency of the wire, which can be detected by a magnetic gap. Calibration of the instrument provides a linearity factor k between output signal and real force. The displacement is recorded with 30 nm precision. For alignment and elongation measurement the apparatus is placed under a stereo microscope. A camera mounted on the microscope can automatically take images every five seconds during the experiment.

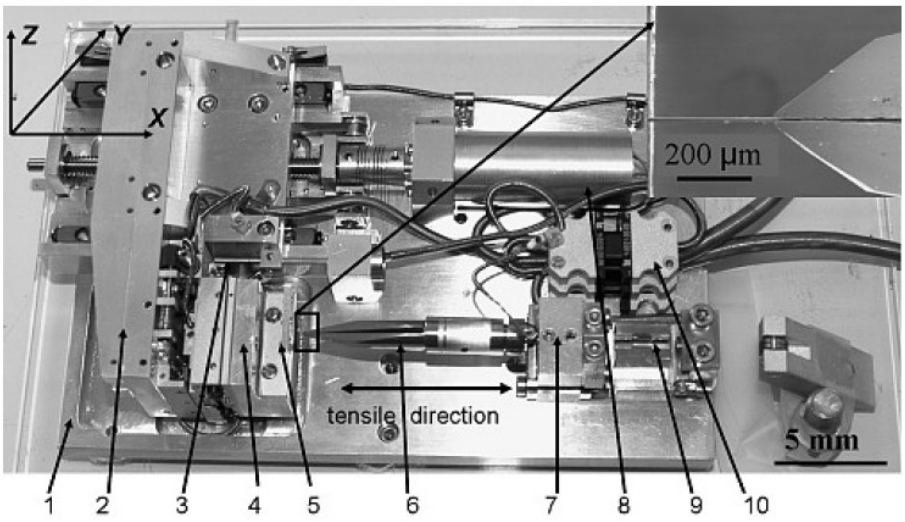

Fig. 13. Photograph of the fibre tensile module with the following components: (1) Base, (2) Main stage, (3) Transformer, (4) Specimen stage, (5) Specimen clamp, (6) Piezo tweezers, (7) Flexible stage, (8) Motor, (9) Magnetic gap, (10) Controller connector [49]

Samples are clamped and fixated on the moveable stage of the apparatus. The sample can be moved in the different directions to place the tensile specimen in axis. The height adjustment is done by varying the focus height of the stereo microscope. On the other side piezo actuated tweezers are mounted. The tweezers close to zero displacement to clamp the head of the tensile specimen. Alternative to the piezo tweezers, the specimen head can be glued with conductive carbon cement (CCC) on a piece of silicon wafer.

Since the apparatus only provides the force and displacement data, stress and elongation have to be calculated. To calculate the stress, the area of the cross section of the tensile specimen has to be measured. This can be done by measuring the fractured cross section from a micrograph, either taken under a light microscope or in the SEM. For the calculation of the elongation the gauge length is essential and can be measured before the experiment under a light microscope and from the photographs during the experiment.

3. Experimental

A detailed description for the preparation of thin sections of wood for laser application is given in the following section. First, tests were performed to find laser parameters suitable for processing of wood. Experiments with different geometries showed limitations regarding the size of machined samples. Since the laser spot has a diameter of 20 to 30 µm, the processing of a defined sample geometry is only possible for samples of the same or greater size. Therefore, compressive and tensile samples with a cross section of around 70 x 60 μm^2 were machined.

3.1. Sample preparation

In this section the steps necessary for laser processing of wood samples starting from a tree are described. Wood pieces were already cut and stored at the Institute of Wood Technology and Renewable Materials of the University of Natural Resources and Life Sciences, Vienna. The institute is located in Tulln in Lower Austria. Furthermore, the thin sectioning, employing a microtome at room temperature, was performed there. The subsequent steps for preparation of the thin sections for laser processing are described.

3.1.1. From a tree to a thin section

The processed wood comes from an over 100-year-old Norway spruce (Picea abies). A small piece was cut from the outer region of an already cut and dried board. Before using the microtome, the wood piece had to soak in distilled water for 48 hours. The microtome used was a sledge microtome from the company C. Reichert Wien (Fig. 14). It has a steel knife, which is sharpened with abrasive paste and honed to get a sharp edge. The knife is fixated in the designated clamp on the sledge. The soaked wood piece is clamped on the sample holder with the region of interest parallel to the so-called cutting plane. With an adjusting wheel the sample can be moved upwards and into the cutting plane. Sample and knife should be kept wet to reduce friction. The knife is moved across the sample via the sledge. After every cut the knife has to be moved back to the initial position before the sample is moved upwards again. Scale marks on the adjusting wheel indicate the moved distance, which is at the same time the thickness of the thin section. Water drops on the knife help to straighten the thin section during cutting. The wood sections can be removed from the knife with a brush and put into a plastic container filled with distilled water for storage.

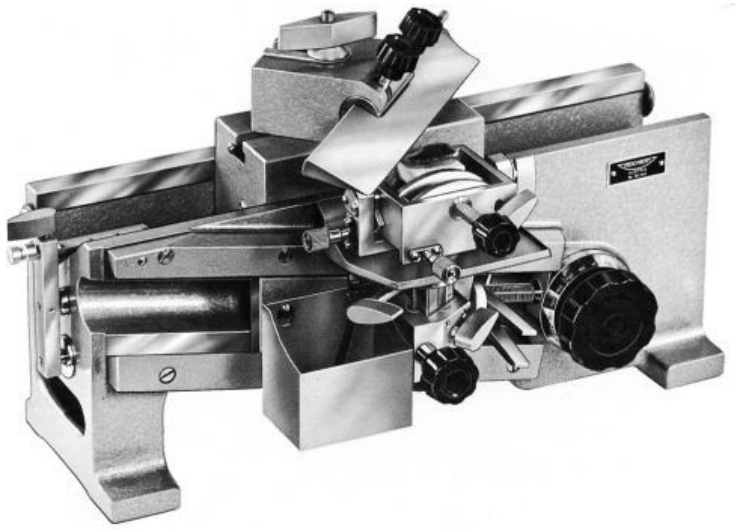

Fig. 14. Exemplary illustration of a sledge microtome from company C. Reichert Wien [50]

The cutting can be performed in the desired directions and for the desired thicknesses. The thickness can be varied between 50 and 200 µm. With thinner sections the wood starts to crumble and would have to be embedded. Thicker sections are not possible because the knife would get stuck. The last step is to add a small amount of sodium azide to the thin sections. This chemical is toxic and prevents the wood from fungal decay.

3.1.2. Drying of specimens

Thin sections were delivered in distilled water with sodium azide for conservation. To process the samples in the laser chamber, they had to be dried to avoid outgassing. The drying between glass sheets, which are normally used as microscope slides, is an established preparation technique for wood fibres [51, 52]. In this section a step by step instruction of the drying process is provided.

Materials needed for preparation: glass sheets, paper clip, filter paper, distilled water, beaker glass, paper tissues

Tools for preparation: disposable protective gloves, tweezers, scissor-like tweezers, razor blade, marker pen

- Make sure the workspace is clean and tidy. Wear powder-free disposable nitrile gloves. Clean the glass sheets with alcohol. Fill distilled water into the beaker glass. Keep the paper tissues ready for rinsing and drying of the tools.

- Carefully open the plastic container with the thin sections in it. Maybe pour some of the conservation solution into the chemicals drain to prevent the container from overflowing.
- Now use the tweezers to grab one of the thin sections and take it out and put it into the beaker glass. Here, the scissor-like tweezers might be helpful.
- Now firmly close the plastic container with the remaining thin sections and put it safely aside.
- Rinse the thin sections in the distilled water. Use the tweezer and move the thin section around in the water. This step is important to avoid salt grains from the sodium azide after drying.
- Keep the cleaned glass sheets ready. Put the first thin section with the concave side onto the glass. The surface tension of the water will straighten the section. Use the filter paper to soak up excessive water. Be careful that the thin section does not get stuck on the filter paper. Do not use paper tissues for this purpose.
- Now use the razor blade to cut the thin section into smaller pieces. If the sample is broader than around 5 mm, macroscopic cracks perpendicular to the tangential direction will occur. This happens because the latewood is denser than earlywood, therefore its shrinkage is greater and internal stresses arise.
- Now place the second glass sheet on top of the first one. Be careful to not move the glass sheets against each other. The thin sections might slide out from between the sheets.
- Label the glass sheet with orientation and thickness of the wood samples and also the current date.
- Now clamp the glass sheets with one or two paper clips. This helps to prevent further rolling of the thin sections during drying.
- The samples can now dry at room conditions. The humidity will reach the level of the room within a few days.
- The dried samples can be manipulated with tweezers. The room humidity is sufficient for the thin sections to remain tough enough for manipulating.

3.1.3. Mounting for laser ablation

The thin sections have to be somehow fixed during processing in the laser chamber. The first possible assembly is an SEM specimen stub made out of aluminium with a 2 x 2 mm^2 groove

in it. On the top surface of the holder near the edges of the groove two stripes of carbon pads are placed. Now the thin wood section can be placed over the groove. Adhesive glue would not be possible because of outgassing in vacuum during processing. Furthermore, the removal of the glue is normally done with acetone. This chemical would dissolve the lignin in the wood and affect the mechanical properties. Laser processing can take place as if the wood was a free-standing specimen. This procedure was used for the optimization of laser parameters.

For pillar tests a different assembly was used. Since the carbon pad influences the mechanical test results, it was totally banned for compressive testing. An SEM stub was used again, but the thin wood section was directly placed on the aluminium. To fixate the thin section, two corners of the wood were fixed with a drop of conductive silver lacquer.

For the processing of tensile specimens, the thin sections of wood were directly clamped in the holding device of the Kammrath & Weiß tensile module. The thin sections were therefore free-standing specimens and could be easily manipulated.

The specimen stub or holding device is placed on the sample holder. Before inserting it into the laser chamber the sample height is measured to adjust the WD of the laser. The vacuum of 10^{-3} mbar evaporates the remaining humidity and the wood is ready for processing. No special atmosphere is needed. To look at the wood structure in the SEM, the sample is inserted into the main chamber. Because wood is a dielectric material, a low acceleration voltage should be chosen to avoid charging effects and possible beam damage. Such beam damage on wood has already been suggested in literature [53, 54].

After the thin sections have been in the laser chamber, the wood is totally brittle. The vacuum of the laser chamber evaporates all remaining water content and, like other biological materials, wood becomes brittle. After some time at room conditions the wood takes up water from air humidity and gets tough again [55].

3.2. Optimization of laser parameters

There was no prior knowledge what laser parameters would give good results in ablation of wood. Because wood is a dielectric material, ultrashort pulses with high laser fluence are needed for material removal. The laser system at the Erich Schmid Institute provides sufficient laser power.

The first task was to find laser parameters leading to good ablation rates and surface quality. Important was also a sharp edge and narrow kerfs. The laser was operated at a 515 nm wavelength and 50 kHz pulse repetition rate for all tests on wood. The beam was guided with the minimum scan speed of 1 mm/s. The geometry was defined with a CAD software. The parameters which were varied were laser power, divisor, number of passes and WD.

The maximum average power is 1.02 W for the given wavelength of 515 nm and 50 kHz pulse repetition rate. It can be controlled by an integer between 0 and 4096. Zero corresponds to

no power, whereas 4096 represents the maximum power. The values in between are interpolated linearly. Every lens in the path of the laser has a transmission efficiency for the laser light at any given wavelength. The overall transmitted power is about 64 % of the laser output power. For reasons of clarity the power values will only be shown in mW with transmission efficiency included. The divisor determines the fraction of the pulses which are reaching the sample based on the chosen pulse repetition rate. The number of passes or layers defines how often a given geometry is scanned by the laser. Since the ablation depth per pulse is dependent on the laser power but otherwise fixed, this parameter plays a decisive role for the depth of the ablated kerf. The WD respectively height of the focal plane can be varied by the beam expander as described in section 2.2.

3.2.1. Power

The first tests were done with varying laser power. The machined sample was a 50 µm thick cross section of spruce. A set of lines of 250 µm in length were scanned with 10 passes and a divisor of 50. The power was varied between 159 and 383 mW in steps of 32 mW and also 478 and 638 mW.

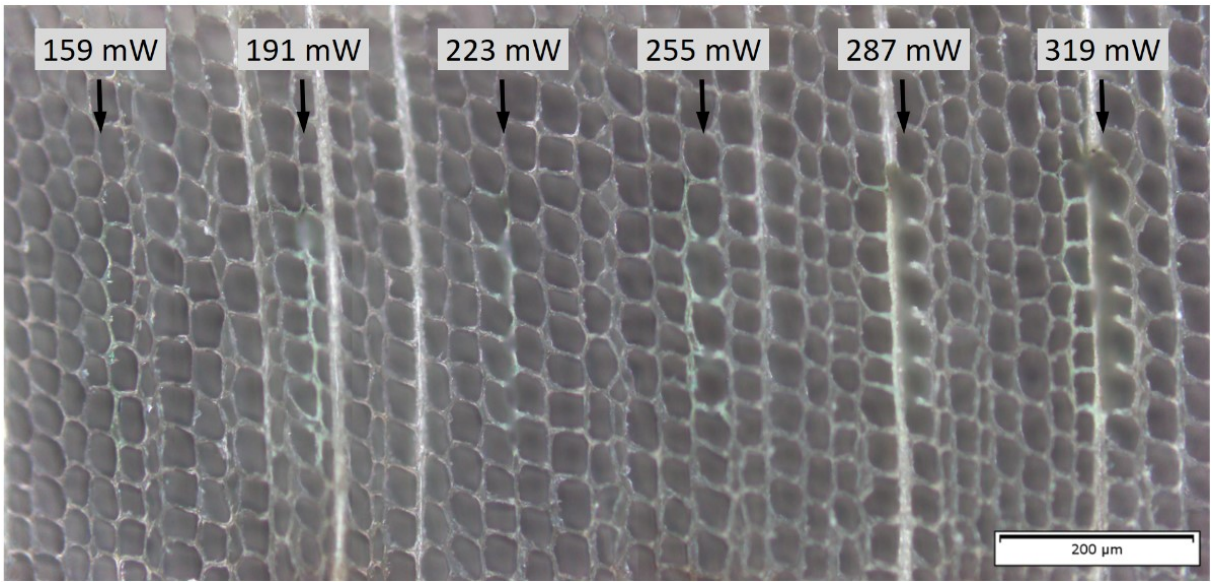

Fig. 15. Optical micrograph with a set of lines cut with 10 passes, a divisor of 50 and different laser power, 159 mW (left) to 319 mW (right); arrows indicate the position of the vertical lines.

Fig. 15 is a micrograph showing the laser kerfs from different power values. At a power of 159 mW, only some surface modification leading to a slight green appearance in the light microscope is evident. For powers of 191 and 223 mW little ablation is visible. Starting from a power of 255 mW considerable ablation took place. For higher powers the ablated kerf got broader (Fig. 16) and even cut through the thickness of the 50 µm thin section of wood.

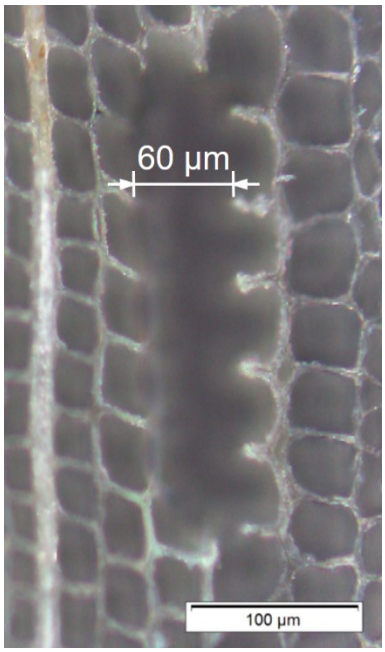

Fig. 16. Optical micrograph illustrating the ablation kerf at maximum power of 638mW, 10 passes, divisor set to 50

Another variation was done with powers from 159 to 271 mW in steps of 16 mW. Two sets of 50 µm long lines were cut. The first set was cut with divisor set to 100, the second with divisor set to 250. The number of passes was 100. Ablation was similar to the first test. No line was cut through the 50 µm thick wood sample.

After these experiments a good measure of laser power was determined as 255 mW. Considerable ablation is happening with good surface quality. With higher laser power the kerf gets more and more broadened.

Laser operation evaporates the irradiated material. This debris is partly carried away by the vacuum pump and partly deposited in the laser chamber similar to a sputter process. Residues on the f-theta lens can reduce the laser power significantly. To find reproducible parameters, a clean lens is essential. After cleaning of the lens, a laser power of 159 mW was a good measure for satisfying performance.

3.2.2. Divisor

As already mentioned the divisor determines the fraction of pulses which are reaching the sample. The chosen pulse repetition rate for the wood experiments was 50 kHz. If this amount of pulses is let through onto the sample, the absorbed energy results in heat accumulation and destroys the material. Even a divisor of 10, meaning 5000 pulses per second, leads to extensive heat accumulation (see Fig. 17).

A set of lines was cut with divisor set to 1, 10, 50, 100 and 250. The laser power was set to 287 mW and the number of passes was 10.

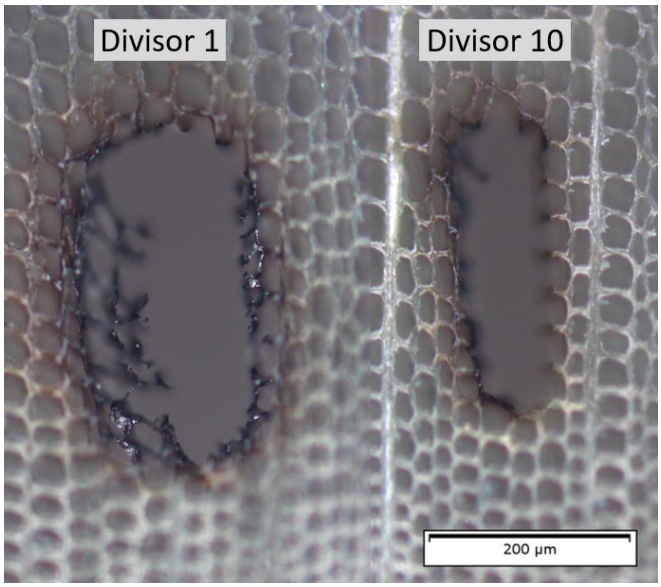

Fig. 17. Optical micrograph illustrating the heat accumulation at divisor values of 1 and 10, which lead to the destruction of the material; power set to 287 mW and 10 passes scanned

With a certain divisor D and the given scan speed v_s, the separation s of laser pulses on the target can be calculated according to equation (3) where f stands for the pulse repetition rate. This was done with different divisor values in Table 1. It was assumed reasonable that this separation should not exceed one fifth of the spot size to get straight edges.

$$s = \frac{v_s \cdot D}{f} \qquad (3)$$

Table 1: Separation of consecutive laser pulses at different divisor values with v_s = 1 mm/s and f = 50 kHz

Divisor D []	Separation s [µm]
1	0,02
10	0,2
50	1
100	2
250	5
300	6

The experiments showed that a divisor of 10 or less lead to significant heat accumulation and destruction of the wood structure. In contrast a divisor of 50 or even more showed good results with a distinguishable edge of the kerf. A divisor of 300 or more would exceed the mentioned limit for a straight kerf edge.

3.2.3. Number of passes

In the first tests lines with 1, 10 and 100 passes were cut at a power of 287 mW and a divisor of 50. In Fig. 18 the focus position of the light microscope was set to the lower surface of the cross section to check if the kerf was cut through the whole thickness. For 100 layers this is the case, whereas after 10 passes the kerf is not cut through.

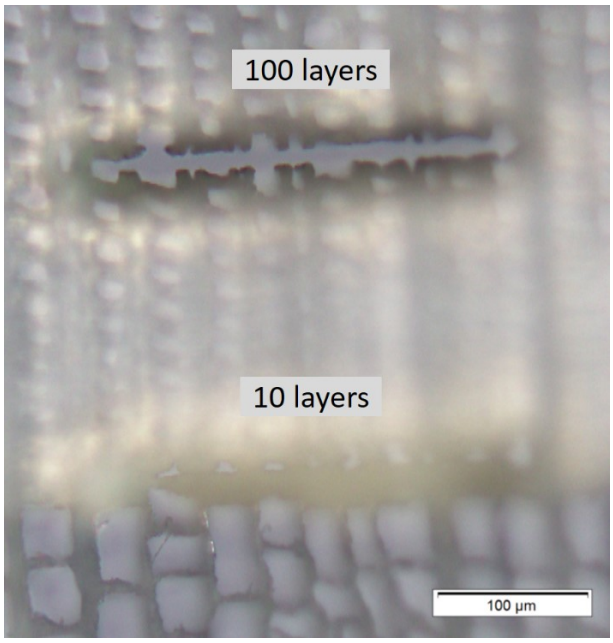

Fig. 18. Optical micrograph of lines with 100 layers (top) and 10 layers (bottom) cut at 287 mW power and a divisor of 50

Furthermore, different numbers of layers were tested for different power and divisor values as well as different geometries, one of which was cutting holes by not moving the laser spot. Active laser ablation was stopped after different long periods. Afterwards not only the time or number of pulses leading to a hole through the thin section but also the size of the ablated region could be measured.

3.2.4. Working distance

The laser spot should be focused on the sample surface. Since the mounted sample has a certain height, this must be considered for the adjustment of the WD. It is determined by the lens distance (LD) in the beam expander. As this distance is the controllable parameter during operation, LD will be given in the following section.

For initial tests, lines with 250 µm length were cut with 287 mW laser power, 100 passes and a divisor of 100. The LD was varied between 10.1 and 9.1 mm (see Fig. 19). A distinctive kerf was visible at an LD of 9.7 mm. As LD was further decreased, the kerf got narrower.

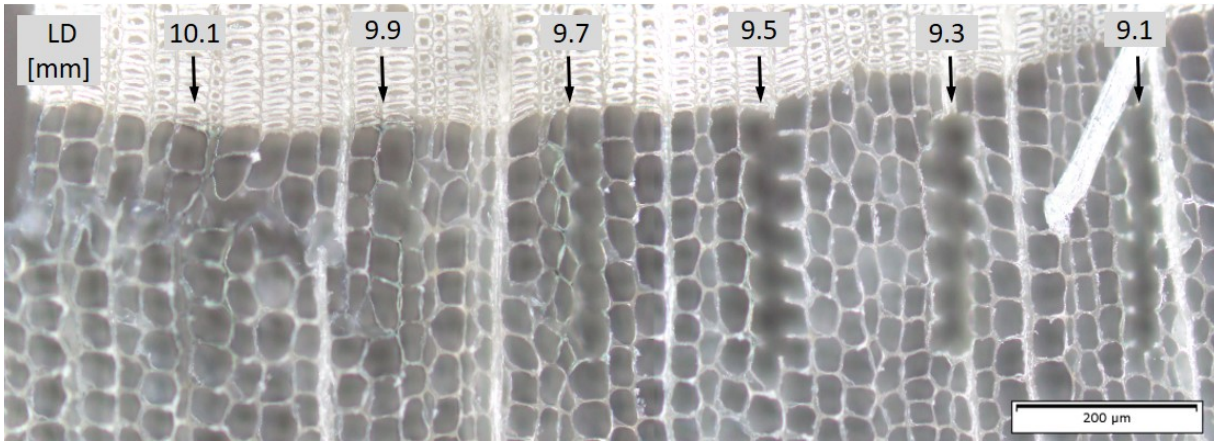

Fig. 19. Optical micrograph with variation of the lens distance (LD) of the beam expander, 287 mW laser power, 100 passes, divisor 100

Another method was to ablate holes similar to layer variation. In Fig. 20 the ablation pattern of points in vertical arrangement with varying LD is shown. Every set of points was cut with a power of 319 mW and a divisor of 250. The ablation time for every point was 20 s.

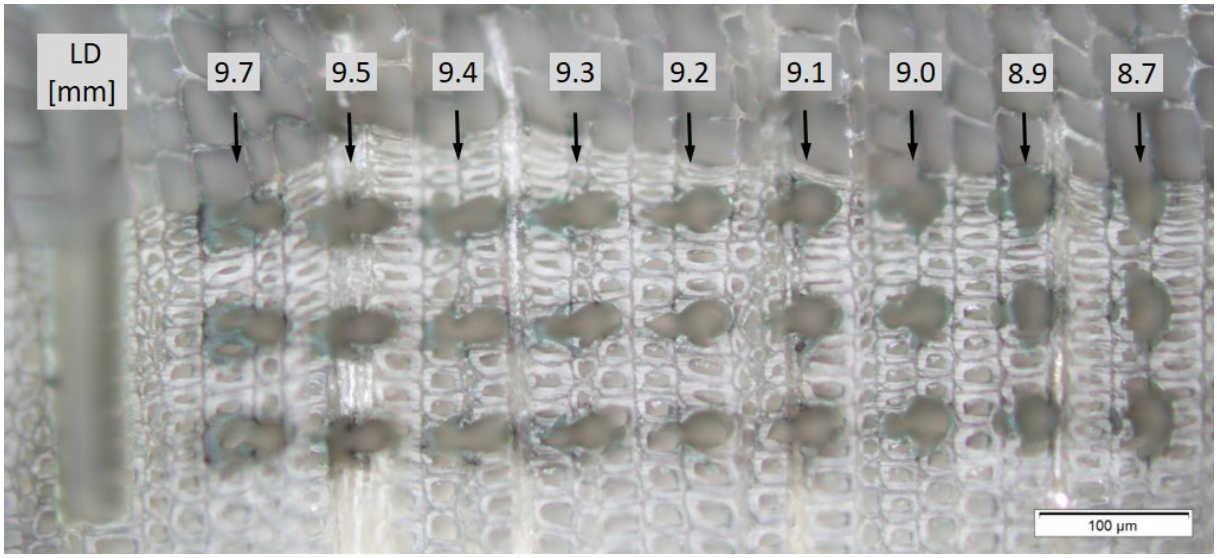

Fig. 20. Optical micrograph of holes cut with different LD, power was 319 mW, divisor set to 250, ablation time of 20 s; a second ablated hole at every position is visible.

The laser spot should have a round shape if the sample is at the focal position of the laser. From the micrograph the distortion of the spot at different LD is visible. A second hole to the left of the original laser position is evident in Fig. 20 and originates from a misalignment of the lenses in the beam expander. After a correction of the misalignment a better laser spot was achieved.

3.3. Cutting of pillars

Samples for pillar compression were cut from 200 µm thick sections of wood. Since the flat punch indenter has a diameter of 200 µm, a ring-shaped cavity with greater dimension had to be cut. The laser geometry was a set of concentric circles with 10 µm variation of diameter each. Diameters from 260 to 60 µm for rough machining and 50 to 20 µm for fine machining were cut. Different laser parameters were used to cut eight sets on cross and tangential sections respectively. Because of the cellular structure of wood, it is a matter of chance to get a free-standing pillar as desired.

The testing of pillars with the G200 nanoindenter was not observable during the experiment, because the instrument switches between indenter and microscope. The tested pillars were imaged before and after the experiment in the SEM.

3.4. Tensile specimens

3.4.1. Processing with ultrashort laser pulses

For the cutting of tensile specimens wood sections were clamped in the same holder as for the tensile testing module. The clamp was fixed on a vice for laser processing and the sample height was measured for determination of the WD. On the first wood section different parameter sets were tried. Before a second batch of samples was cut, the entry window of the laser chamber was cleaned. After that the transmitted power was higher than before. A new, more accurate parameter set was determined as shown in Table 2.

Table 2: Final parameter set for preparation of tensile specimens

Laser wavelength	Pulse repetition rate	Lens distance	Scan speed	Divisor	Power	Layer	Scan repetition rate
λ	f	LD	v_s	D	P	L	S
515 nm	50 kHz	7.8 mm	2 mm/s	25/40*	398/159 mW*	3	4

*parameters after initial tests and after cleaning of the entry window

Number of passes or layer determines how often every single line is scanned before moving to the next one. In contrast to that, the scan repetition rate *S* determines how often the whole geometry is scanned. A scan speed v_s of 2 mm/s and a divisor of 25 is equivalent to

v_s = 1 mm/s and divisor of 50 in terms of laser pulses per scanned length. The big advantage of higher scan speed is the decreased processing time.

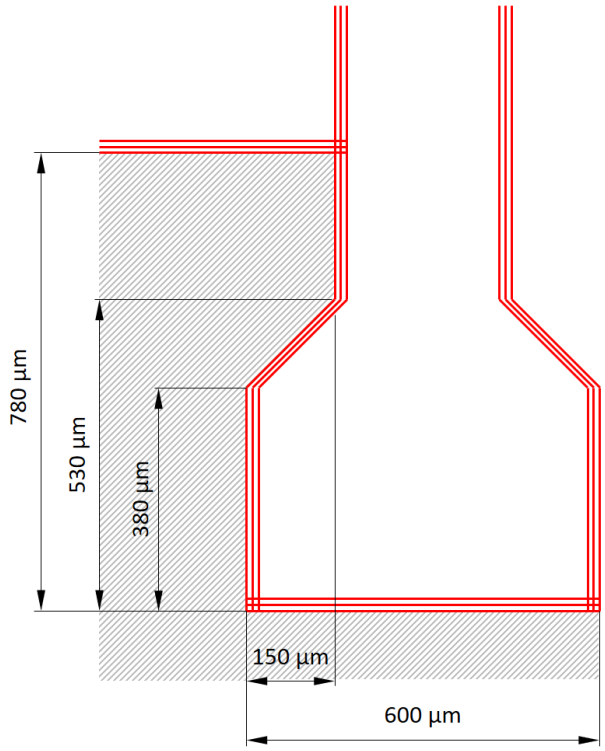

Fig. 21. Geometry for laser cutting of tensile specimens; the shaded region indicates the remaining material after cutting.

Fig. 21 shows the geometry for laser cutting imitated from the copper samples of Smolka et al. [44]. A sequence of three lines, separated by 10 µm, was scanned to increase the kerf. After around one minute of laser cutting the surplus material fell down. The remaining material is indicated as shaded regions in Fig. 21. After every cut-out the geometry was moved 685 µm, so that the remaining width of the free-standing tensile samples was about 70 µm.

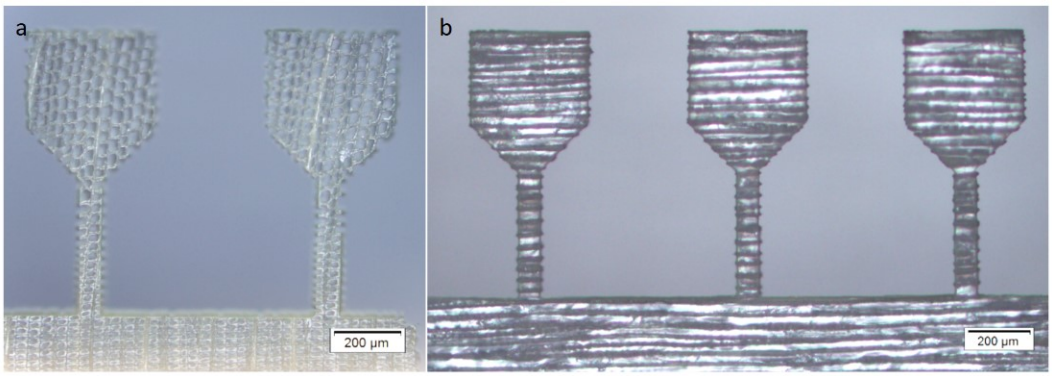

Fig. 22. Optical micrographs of tensile specimens on a cross section (a) and a tangential section of wood (b)

Tensile samples were cut from cross sections in radial and tangential direction, as well as perpendicular and parallel to the grains on tangential sections (see Fig. 22).

3.4.2. Tensile specimens produced by ion milling

Alternative to the laser processing, tensile specimens were produced with the E-3500 ion milling system and a copper mask.

A thin section was placed onto the sample holder. A section with an array of six copper tensile specimens was cut from the wafer. The side with the copper film was placed on top of the wood section. Two clamps fixated the wood section with the mask (see Fig. 23). The sample holder was fixed on the X-Y stage and placed under a light microscope. Here the sample could be moved by the stage, so that the ion beam hit the desired region. After that the stage with the sample was inserted into the ion milling system.

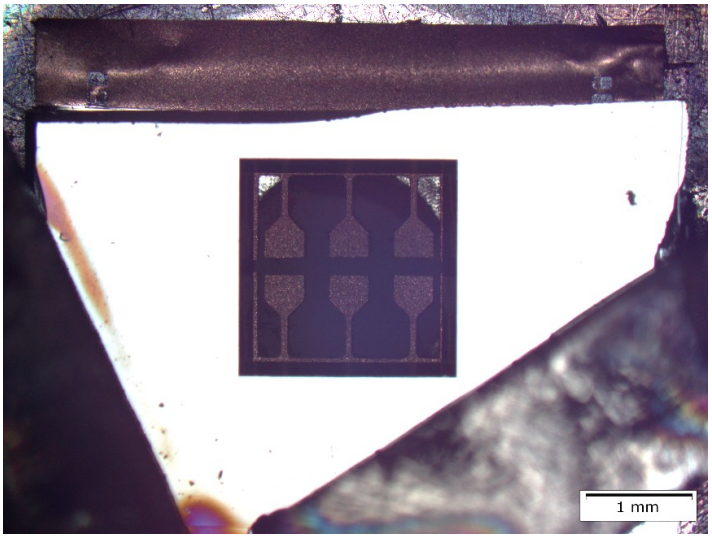

Fig. 23. Optical micrograph of the Cu-mask with already etched wood underneath

The used parameters for ion milling were 4 kV discharge voltage and 2 kV acceleration voltage. The stage rocking was turned off and the discharge current was kept constant at 300 µA by regulating the gas flow. The beam centre was placed between the dumbbell-shaped tensile samples of the mask and moved after 30 min etching each. After about three hours the wood was etched away. The mask could only be used once because the thickness of 20 µm was also eroded after the etching.

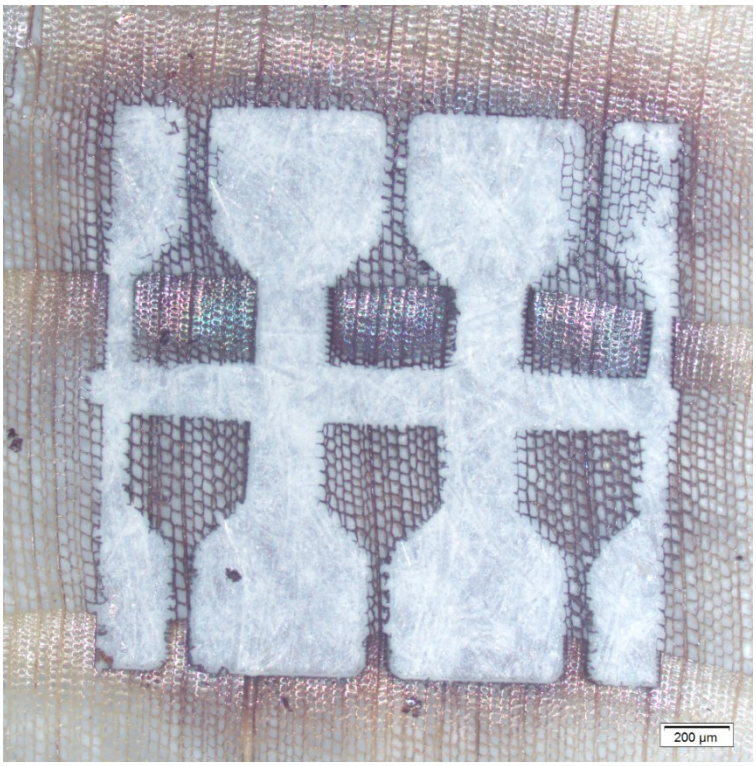

Fig. 24. Optical micrograph of an array of six tensile samples after ion irradiation; the colour change at the edges is apparent to the naked eye.

Fig. 24 is a micrograph of an array of six tensile specimens. The change in colour and the black appearance at the edges indicate that the wood seems to have been carbonized during ion irradiation. Not only at the edges but also in regions under the mask the wood is clearly affected.

3.4.3. Performing tensile tests

The tensile specimens had similar geometry for laser processing and ion milling. One side was clamped on the moveable stage of the fibre tensile apparatus. The free-standing heads of the tensile samples could be gripped either by the piezo actuated tweezers or glued with CCC on a fragment of a silicon wafer.

A problem with the actuated tweezers is the obstructed view on the sample. If the sample is not at the exact height, the tweezer causes the tensile specimen to bend and fracture before the experiment starts. The distinction of the sample height or gripper height can be found by the focus position of the stereo microscope. Since one tweezer jaw remains at the same position, the sample can be slowly approximated and then gripped. Unfortunately, the gripping causes deformation of the underlying material and introduces a pre-stress on the samples. After the experiment the gripped head sticks to the tweezer jaw because of adhesion. It can be swiped away with an eyelash gripped with manual tweezers.

For fixation with CCC the sample is approximated to a piece of silicon in the same way as for the piezo tweezers. To fix the head of the sample a drop of CCC is placed right next to it with a wire. After 20 to 30 min the CCC has hardened and the experiment can be performed. In this arrangement the specimen is fully observable and a bending momentum can be avoided. Another advantage is that both sample pieces can be retrieved whereas the sample head is lost when using the piezo tweezers.

The tests were performed with a speed of 0.5 µm/s. A camera mounted on the stereo microscope automatically took pictures every five seconds.

3.5. Compression samples for the fibre module

3.5.1. Laser processing

The cutting of pillars as described in section 3.3. was time consuming with low output of useable samples. Furthermore, the compression experiment could not be observed simultaneously. Therefore, compression samples were cut from thin sections in the same manner as tensile samples. Laser parameters were the same as described in Table 2 and the cutting geometry is shown in Fig. 25. It was designed to get samples with 70 µm width and an aspect ratio of 2:1. The whole geometry was moved 870 µm to the left to get two new samples.

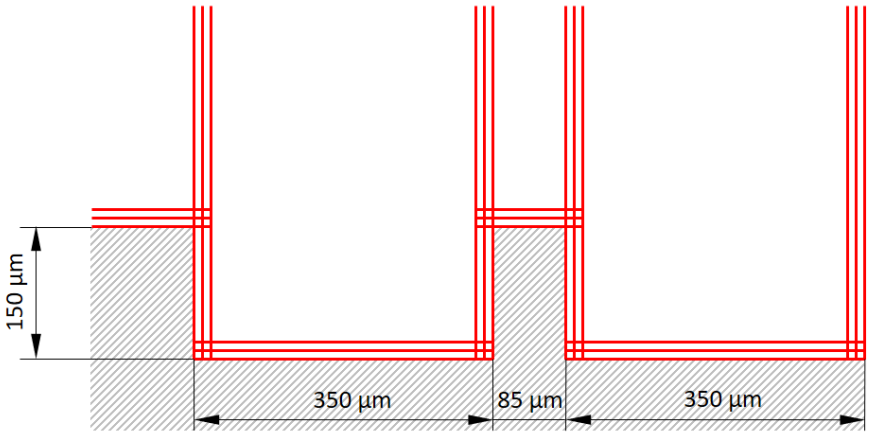

Fig. 25. Cutting geometry for laser processing of compression samples; shaded regions indicate the remaining material.

3.5.2. Compression tests with the fibre module

For final compression experiments the same apparatus as for tensile experiments was used. The samples were clamped and fixed in the same way on the moveable stage. As an indenter the shaft of a high-speed-steel drill with 0.5 mm diameter was used (Fig. 26). The experiment was displacement controlled and the compression force was recorded. The maximum force is limited by the pre-stress of the wire in the magnetic gap. Compression tests were carried out with 1 µm/s test speed.

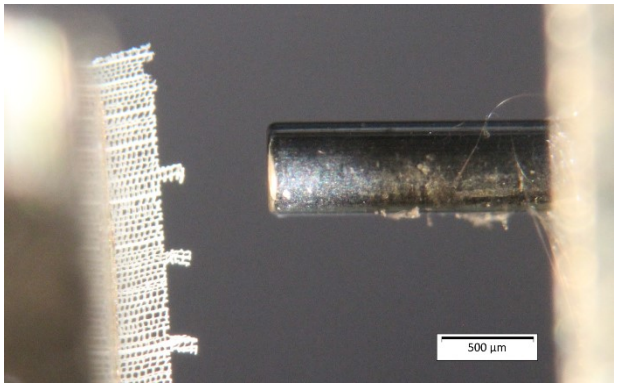

Fig. 26. Optical micrograph of the indenter in the proximity of tested compression samples

4. Results and discussion

Various experiments on wood with different sample sizes have been performed in preceding studies. For example, Futó investigated fracture behaviour of spruce wood under the light microscope. Tensile tests of microtomed samples with 20 to 250 µm thickness and 2 mm width were performed in different directions [56]. For larger magnifications the SEM became a widely-used instrument. It allows for a detailed analysis of the fracture surface as well as performing in-situ experiments [3, 54, 57]. The machining of micrometre-sized samples is vulnerable to damage and the obtained results are questionable, e.g. conventional machining with blades leaves a deformed surface layer. It was already suggested in literature to use laser ablation for removing this structurally damaged layer [58]. However, no such experiments were found in literature. Single wood fibres can be mechanically isolated and are therefore under intensive investigations [5, 6, 59, 60].

The conventional preparation techniques leave a gap in the range of tested sample sizes. Either single wood fibres or specimens with only one dimension at the micrometre scale are tested. The preparation of samples with ultrashort-pulsed laser ablation seems to close this gap of not yet achieved sample dimensions.

4.1. Failure mechanism in tension described in literature

According to Côté and Hanna three types of cell fracture for longitudinal samples are recognized (Fig. 27). First, intercell failure is the separation at the middle lamella. Second, intrawall failure happens within the secondary cell wall, usually at the interface between S_1 and S_2. Third, transwall fracture propagates across the cell wall [61].

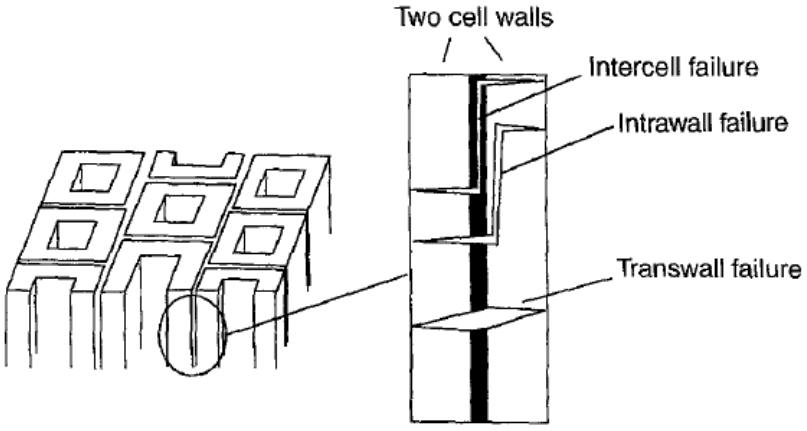

Fig. 27. Schematics of the three different failure types in longitudinal direction according to Côté and Hanna [3]

Dill-Langer et al. investigated the tensile fracture behaviour in-situ under a confocal laser scanning microscope on cross sections. They found a difference for the failure mode in the different loading directions. In radial loading direction a crack propagates through cell wall rupture, whereas in tangential loading the tracheid fibres debond and the crack leaves a smooth fracture surface. Fig. 28 shows the simplified model for a softwood cross section with illustrated failure modes in the different loading directions. The softwood tracheids are modelled as hollow tubes and resemble a brick wall structure. In radial loading direction, this structure compels a crack on a jagged path leading to rupture of cell walls whereas the crack can follow along a straight line between the cells in tangential loading. [62]

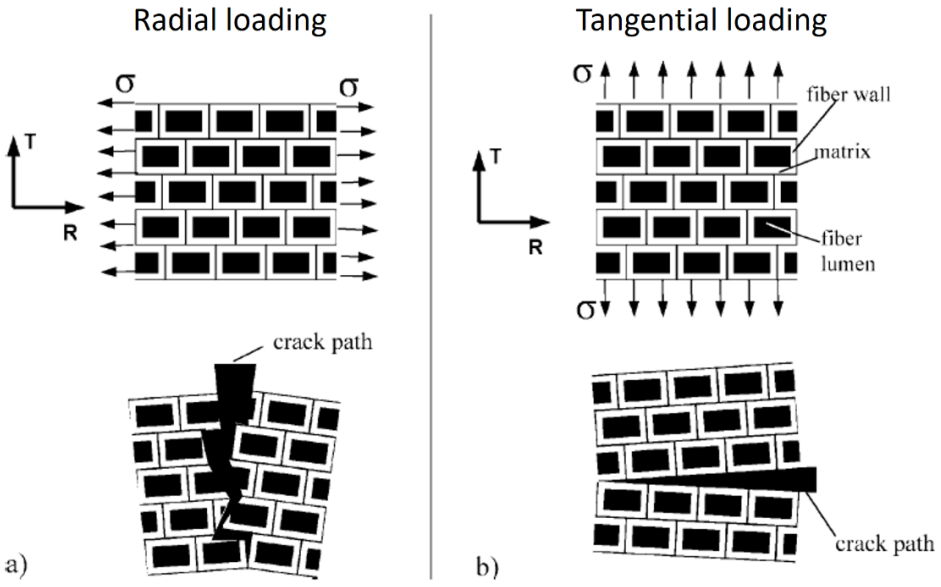

Fig. 28. Simplified morphological model of a softwood cross section and crack propagation for radial and tangential loading [62]

4.2. Observed failure mechanism in tension

4.2.1. Loading in longitudinal direction

Fig. 29 shows a typical force displacement diagram for the tensile test of a longitudinal sample. The small cell wall thickness, visible from axially cut cells on the thin section, indicates that the sample originates from an earlywood region. It shows an almost completely linear behaviour until a crack initiates (see Fig. 29b). Shortly after crack initiation the sample fails abruptly and the force drops to zero. A crack is not always visible. However, every sample has a deviation from the linear behaviour before the sample fractures.

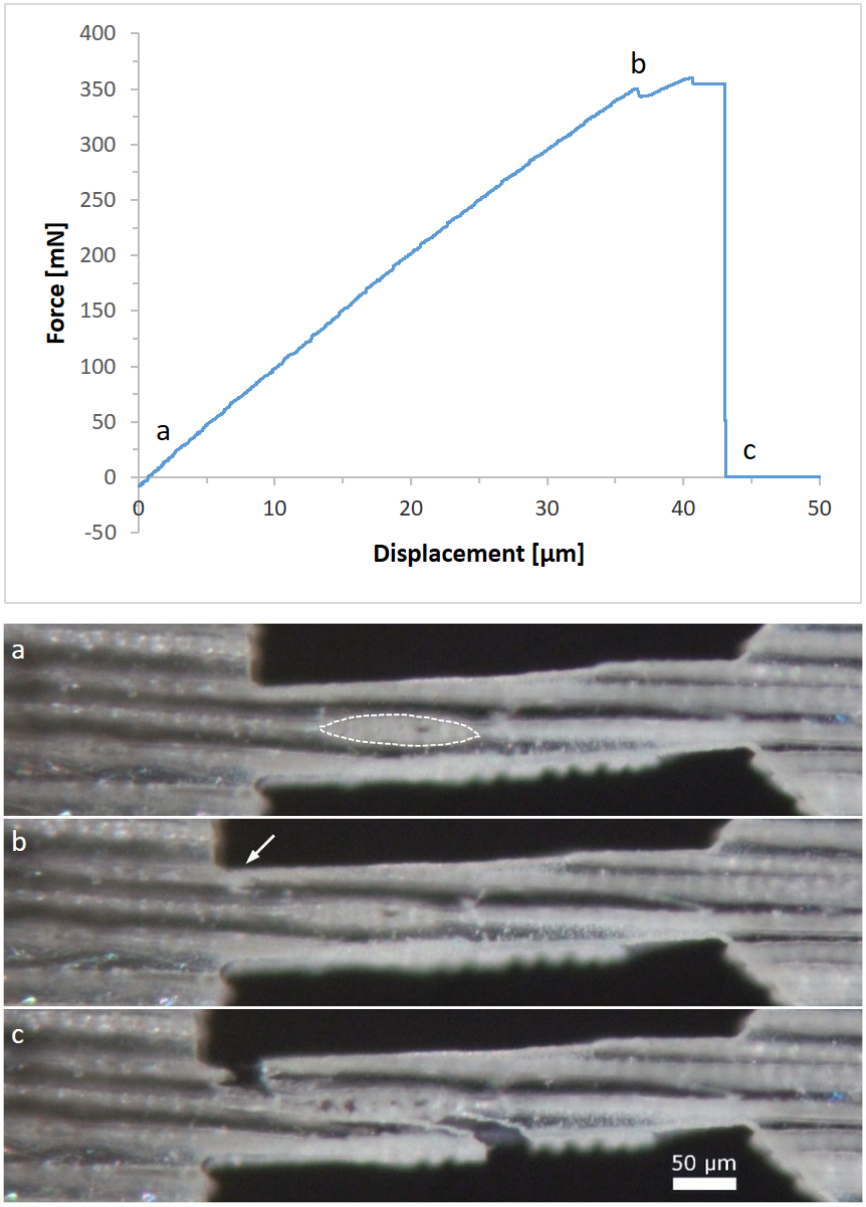

Fig. 29. Typical force displacement diagram of a longitudinal sample, the optical micrographs below are taken at the marked points a-c; (a) specimen before any displacement is applied, the area of an intersecting wood ray is indicated by the dashed line; (b) the onset of a crack is indicated by an arrow; (c) fractured specimen

The fracture surface is serrated and follows in large parts most probably the MFA. Another weak point in longitudinal samples is the interface to wood rays, as can be seen in the example in Fig. 29. Kifetew et al. performed tensile tests on green specimens compared to samples in a dried and resoaked state. The most dominant failure mode in their study for dried/resoaked specimens was transwall fracture [3]. Sippola and Frühmann performed in-situ tensile tests in an environmental SEM. They observed crack propagation in longitudinal direction before transverse cracking occurred. Local differences in material strength were identified as weak spots. The dominant failure mode is intrawall fracture with occasional intercell failure. Ex-situ

fracture experiments revealed identical fracture surfaces [57]. It seems that the drying process has significant influence on the fracture behaviour.

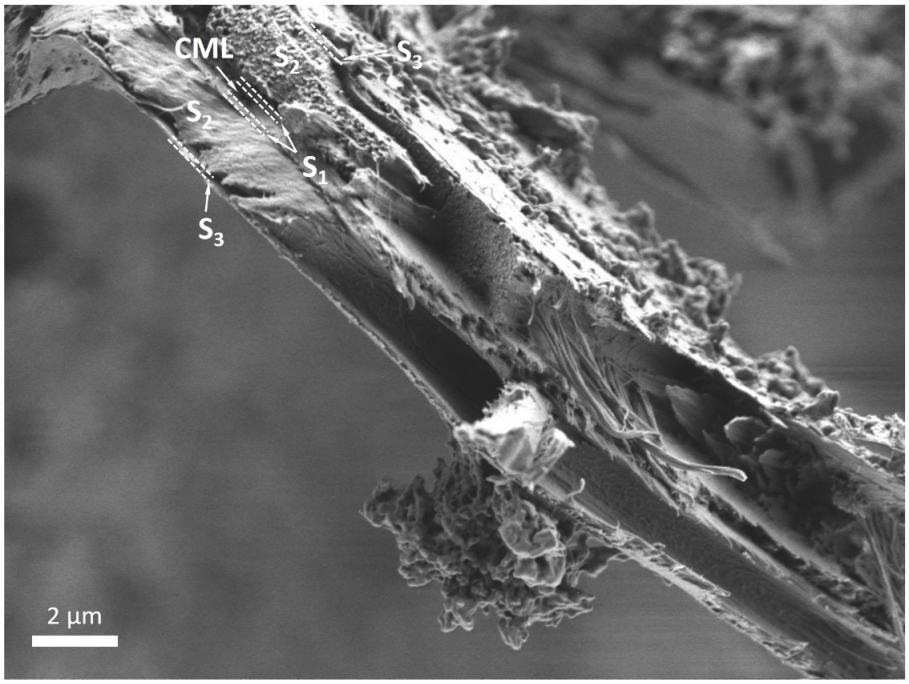

Fig. 30. SEM micrograph of a fracture surface section of a longitudinal sample viewed in loading direction; the different cell wall layers are indicated, the compound middle lamella (CML) consists of the primary wall and the middle lamella; crack propagation in the S_2 layer was along the MFA and failed microfibril packages alternately.

Fig. 30 is a micrograph of a fracture surface section of a longitudinal sample in the SEM. The fractured surface shows a serrated S_2 layer. The crack propagated along the direction of microfibrils and alternately failed microfibril packages.

4.2.2. Loading in radial and tangential direction

In this study the same two different failure regions can be distinguished as described by Dill-Langer et al. [62]. Most often the samples fracture through the cell wall. This seems reasonable since the loading direction is in the weak direction of the S_2 layer. In Fig. 31 a fractured radial sample is shown. Some microfibrils still stick to both fragments.

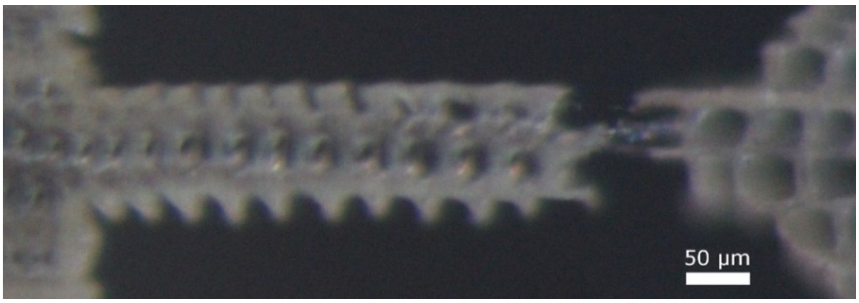

Fig. 31. Optical micrograph of a fractured radial sample with microfibrils still connecting the two fragments

Fig. 32 shows a fracture piece of a radial sample viewed in the SEM with 1 kV acceleration voltage. The sample fractured through the cell wall. In the bottom half of the image, delamination of the middle lamella off both adjacent cells is visible. The S_3 layer ruptured with the rest of the cell wall and is still intact at the visible lumen area. The grainy appearance on both sides of the sample originates from laser cutting.

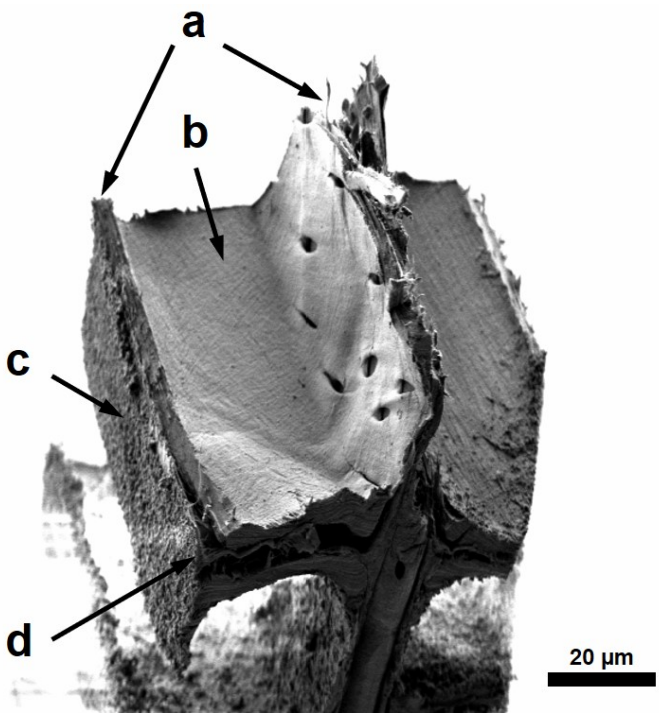

Fig. 32. SEM micrograph of a fractured sample loaded in radial direction; (a) rupture of the cell walls, (b) still intact S_3 layer at the lumen area, (c) laser-processed surface, (d) delamination of the middle lamella

In contrast to that, some samples separated between the wood cells. This second failure mode is called fibre debonding. Fig. 33 shows the force displacement diagram of a tangential sample. The micrographs taken at different displacements are depicted below. The negative force at the start of the experiment is a result of the clamping with the piezo tweezers. The material of the sample head yields under the tweezer jaws, which can result in elastic deformation

and/or bending of the sample. The first peak in the force displacement curve, marked with (b), results from the breaking of a single cell wall. This is marked with a white arrow in Fig. 33b. The major force drop corresponds to a separation at the middle lamella between four adjacent cells (white arrow in Fig. 33c). With further displacement the cells are pulled apart, showing a rhomboidal shape, before one connection breaks. With the remaining displacement the S_3 layer of the remaining single cell wall is pulled off.

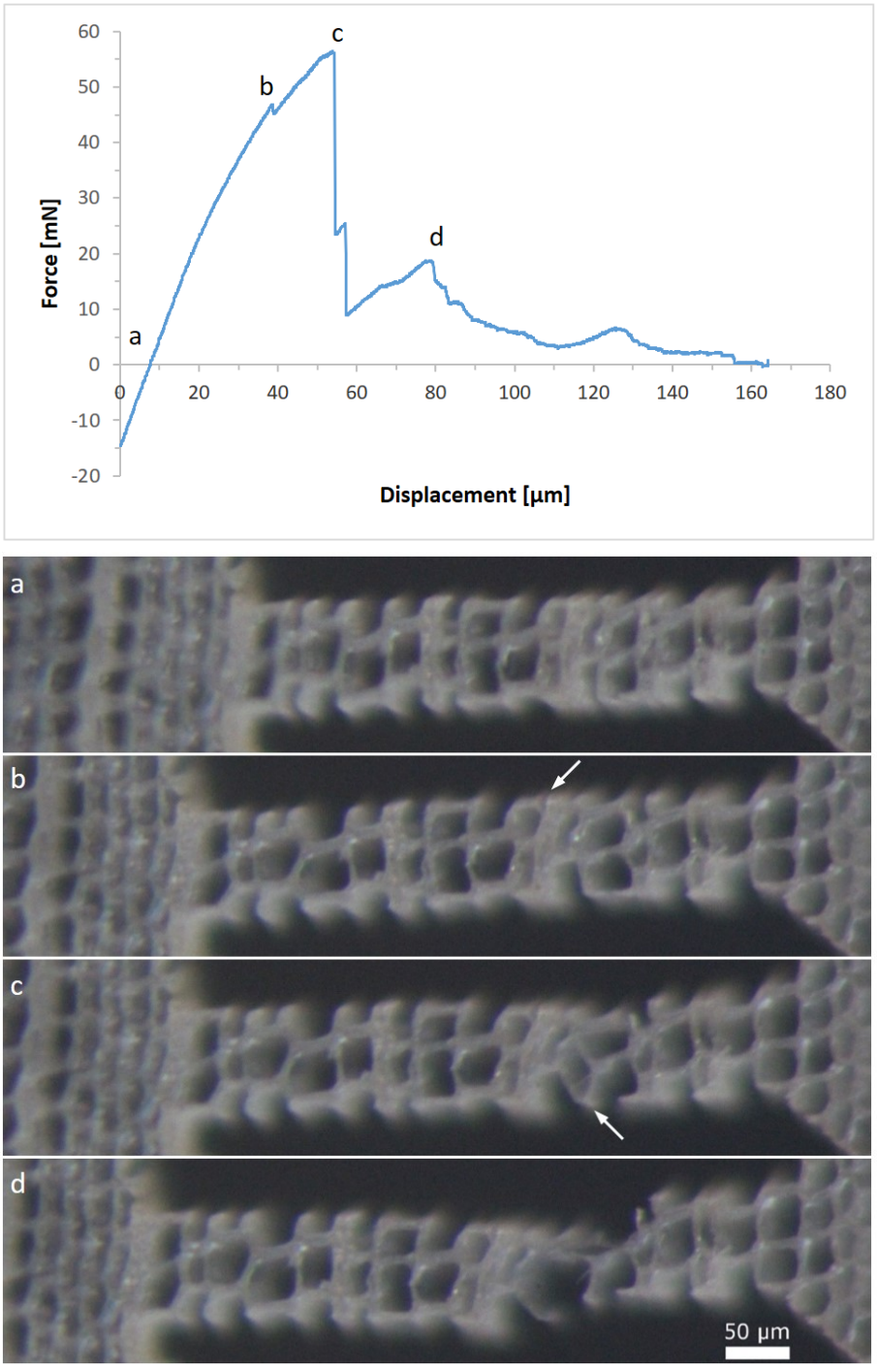

Fig. 33. Force displacement diagram for a tensile test in tangential direction; the optical micrographs below show the sample corresponding to loading stages a-d; (a) unloaded specimen; white arrow in (b) indicates cell wall rupture; white arrow in (c) indicates fibre debonding; (d) rupture of the remaining connection

One sample showed a combination of cell wall rupture and fibre debonding. In contrast to Dill-Langer et al., most tangential samples in this study fractured through the cell wall and not between cells. The reason for this might be the sample geometry. As seen in Fig. 28, the wood cells resemble a brick wall structure. The small sample size in this study however leaves only one to three cell walls in loading direction across the sample width. Cut cells have loose cell walls at the edge of the sample, which cannot transfer the applied load. Fracture happens at the weakest part of the sample, which are the single cell walls. Larger samples might fracture more frequently by fibre debonding since the intact S_1 and S_3 layers give the cells more mechanical stability.

4.3. Quantitative analysis of tensile tests

In this section an estimation of the ultimate tensile strength of the samples is given. However, with biological samples there is a large variation of the local strength of the material and therefore the measured data. In literature variations are attributed among others to damage that occurred during preparation with the microtome [3].

4.3.1. Error estimation

For the calculation of stresses, a few aspects should be taken into account. First, the evaluation of measured force data requires a calibration of the tensile module. For this purpose, two weights with 10 and 20 grams were lifted with the stage. With these two measurements a linearity factor k between measured and true force was determined. Nevertheless, a measurement uncertainty of 2 % should be taken into account.

Second, the resolution of the tensile module was determined by the variation of force value with no sample attached. The variation was 0.046 mN, which is less than 1 % of measured forces. The variation of displacement was 0.026 µm, which is negligible for these experiments.

Third, for evaluation of maximum stress, the force value has to be related to the fractured surface area. Measuring the area is difficult because of the cellular structure of wood. The fractured surface is rough and the focus depth of the light microscope is insufficient, even with multifocal recording. For the estimation of fracture area, the thickness of the fractured cell walls is measured at the light microscope prior to tensile testing. Images were taken at a magnification of 100. Therefore, a deviation of one pixel already means an error of 10 % for the cell wall thickness and around 1 % for the thickness of the thin section. The area was estimated as one or more rectangles with the thickness of the thin section times the thickness of the ruptured cell wall (see Fig. 34).

Finally, measurement uncertainty of the stress values adds up to 14 %. For more detailed analysis, the samples have to be imaged in the SEM.

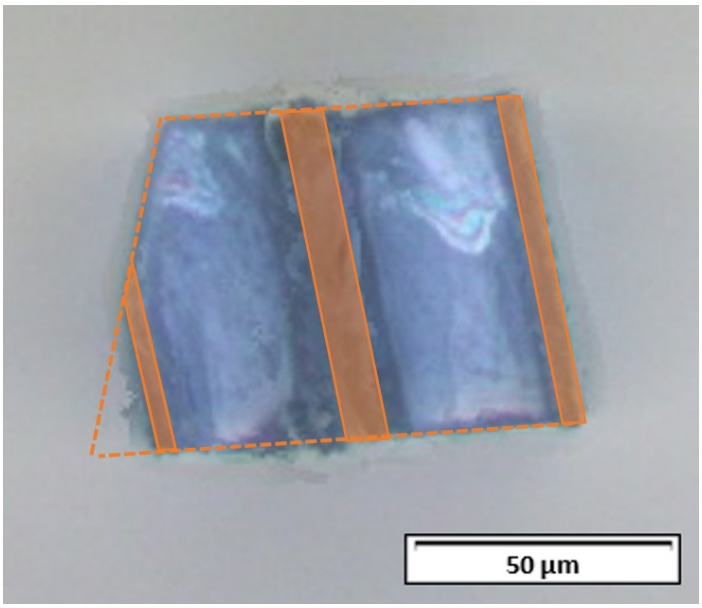

Fig. 34. Optical micrograph of a fracture surface of a radial sample viewed in loading direction; the dashed line indicates the overall dimensions of the sample, whereas the highlighted areas mark the fractured cell walls determining the tensile strength.

For an estimation of the elongation of samples, images taken during the experiment have to be correlated with the force displacement curve to account for the machine compliance.

4.3.2. Tensile strength

It was not possible to measure the fractured cell wall cross section for longitudinal samples because the experiments did not result in a flat fracture surface. However, the force could be attributed to the overall dimensions of the samples. This calculation yields tensile strength of 83 ± 29 MPa, which is comparable to literature [3, 63]. Tensile tests on single wood fibres resulted in measured forces between 120 mN for earlywood to 367 mN for latewood fibres [60]. Since the cross section of the samples in the current study contained on average four earlywood cells, measured maximum forces of 319 to 646 mN seem to be reasonable.

Table 3 shows the tensile strength of cell walls from experiments on different sections. As already mentioned, the calculated stress values have a large error margin. For sections 1, 2 and 4 the standard deviation and for section 3 the error margin of 14 % is shown. The low value for section number 4 could be the result of damage during preparation. For samples on a tangential section of wood with tangential loading direction, no stress values could be

calculated since the cellular structure is only viewable on cross sections. However, the maximum forces correlate well to samples on cross section number 3 in Table 3.

Table 3: Tensile strength of cell walls in transverse direction on different microtomed cross sections

Thin section	Loading direction	Tensile strength [MPa]	Number of samples
1	radial	128 ± 61	2
2	radial	103 ± 22	4
3	tangential	74 ± 10	1
4	tangential	17 ± 4	4

4.3.3. Elongation

In longitudinal direction the fibres are aligned in loading direction and behave almost linearly before fracture. Seven out of nine samples have a fracture strain of 10 to 15 %. Only two samples on the same thin section exhibit a fracture strain of about 5 %.

For samples perpendicular to the cell axis the cellular characteristic of wood has distinctive significance. The hollow fibres resemble a honeycomb. These samples exhibit smaller stiffness in radial direction than in longitudinal direction by a factor of 4. The loading direction has further influence on the strain. In radial direction, the cells are aligned in a row. This means that the applied force is transferred from one cell wall to the next without deflection. In contrast to that, the cell walls in tangential direction are not in line because of the brick wall structure as seen in Fig. 28. Therefore, the applied forces introduce bending of the cell walls perpendicular to the tangential loading. In summary, the displacement to failure depends strongly on the geometry.

4.4. Beam damage

Irradiation with electrons in an SEM causes damage to wood samples as described in literature [53, 54]. To evaluate this, two radial samples were exposed to an electron beam of 1 kV in the SEM before testing. Another three samples on the same thin section had already been tested for comparison. Both electron-irradiated samples fail earlier than the reference samples. The failure mechanism in both exposed samples is fibre debonding (see Fig. 35).

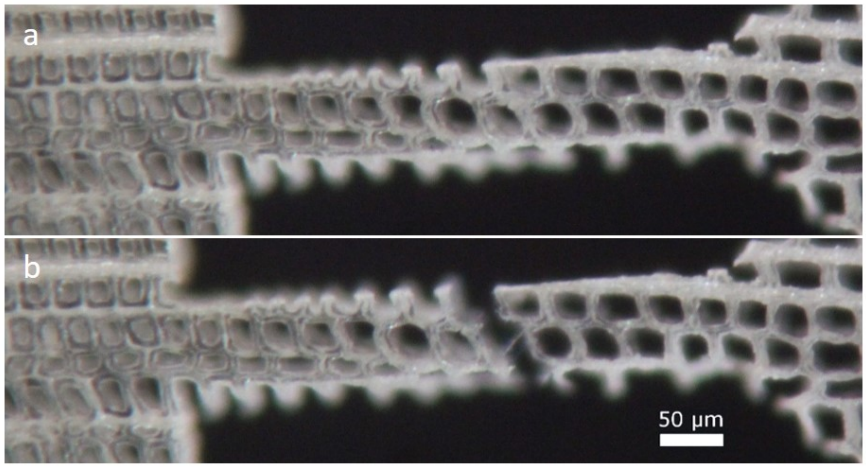

Fig. 35. Optical micrographs of a radial sample exposed to the electron beam in the SEM; (a) unloaded specimen; (b) failure through fibre debonding

The fracture surface is not flat as would be the case for a tangential sample. This means that the middle lamella might be significantly weakened by the electron beam. Fig. 36 compares the calculated stress values for fibre debonding, which happened in two cases of radial and tangential samples, and the exposed samples. The calculated stress of the beam-damaged samples is significantly lower by a factor of 5.

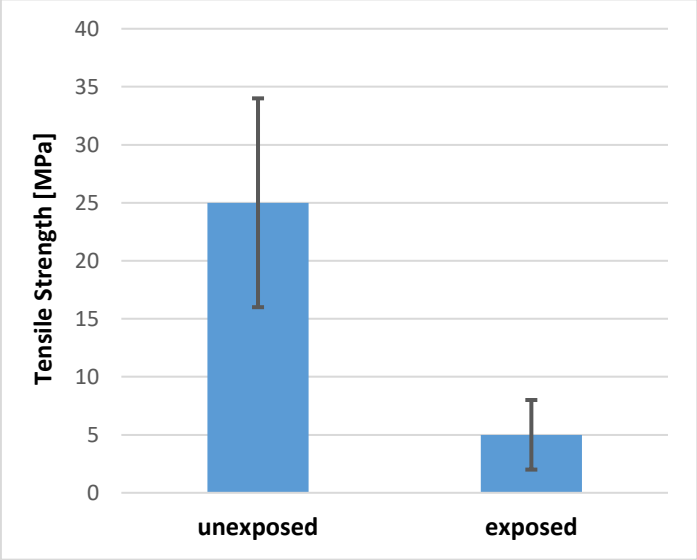

Fig. 36. Comparison of tensile strength of fibre debonding between samples, exposed and unexposed to electrons with 1 kV in the SEM

4.5. Comparison of fs-laser processing and ion milling

The FIB has already been used for preparation of wood pillars and bending beams [7–10]. It is not an alternative because the processing time for samples with the size used in this study would be several days due to the limited ablation rate. However, a possible preparation method for samples in this size range is ion milling with a mask.

4.5.1. Surface quality

The thin sections already have a rough surface after being sliced with the microtome, revealed by the SEM in Fig. 37. Cell walls are frayed and delaminated at the middle lamella. Surface quality might improve with a sharper knife edge. Tokareva et al. investigated different sample preparation techniques for performing secondary-ion mass spectroscopy on wood tissue. They suggest disposable razor blades for sectioning and evaluate different drying methods to get the best surface quality [64].

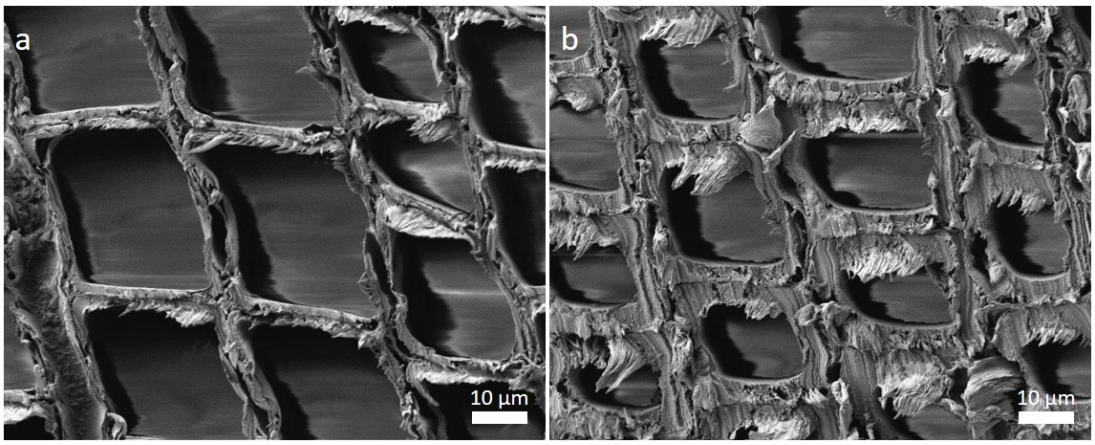

Fig. 37. SEM micrographs of the surface of thin sections after microtome cutting; (a) earlywood and (b) latewood

Sample surfaces after laser processing show a layer of grainy, maybe melted and re-solidified cellulose (Fig. 38). The appearance in this study is almost identical to fs-processed surfaces of other woods as found in literature [40].

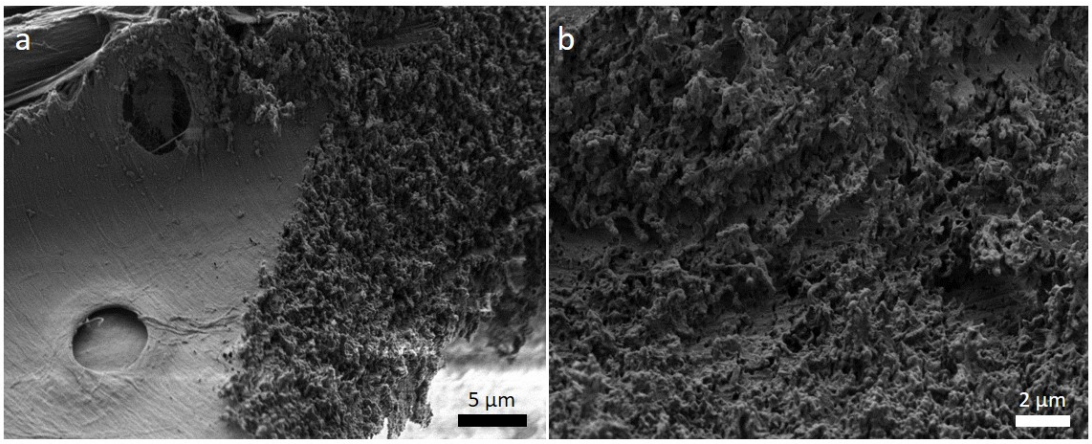

Fig. 38. SEM micrographs of a fs-laser processed surface; (a) next to the laser kerf the intact S_3 layer with pits is visible, (b) larger magnification of the laser incised surface

The samples after ion milling were clearly affected by the ion irradiation, even in regions under the copper mask. This damage was visible to the naked eye in form of a gradual colour change (see Fig. 24 in section 3.4.2.). The black appearance at the edge of the samples may relate to carbonization. Further investigation in the SEM showed features on the surface, which look like melted wood components, even under the mask (see Fig. 39 and Fig. 40).

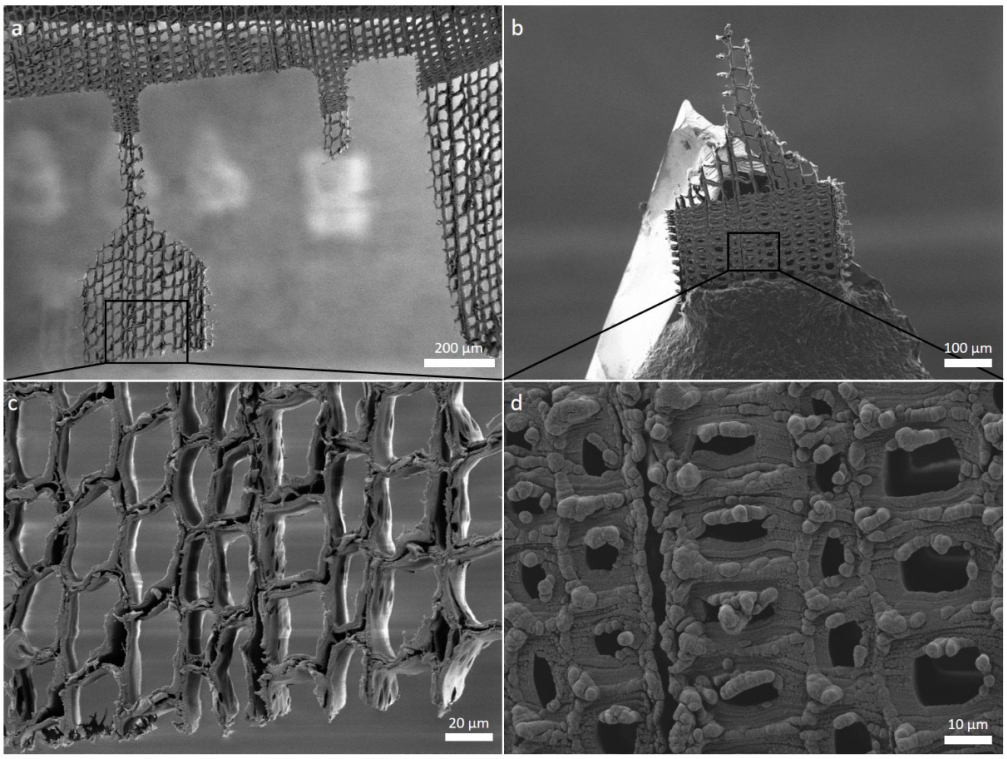

Fig. 39. SEM images of radial samples prepared by ion milling; (a) an untested sample, (b) Sample head glued to a silicon piece with CCC, (c) detail of (a) showing loosely connected wood cells, (d) detail of (b) showing maybe melted wood components on the surface in a region shadowed by the copper mask during ion irradiation

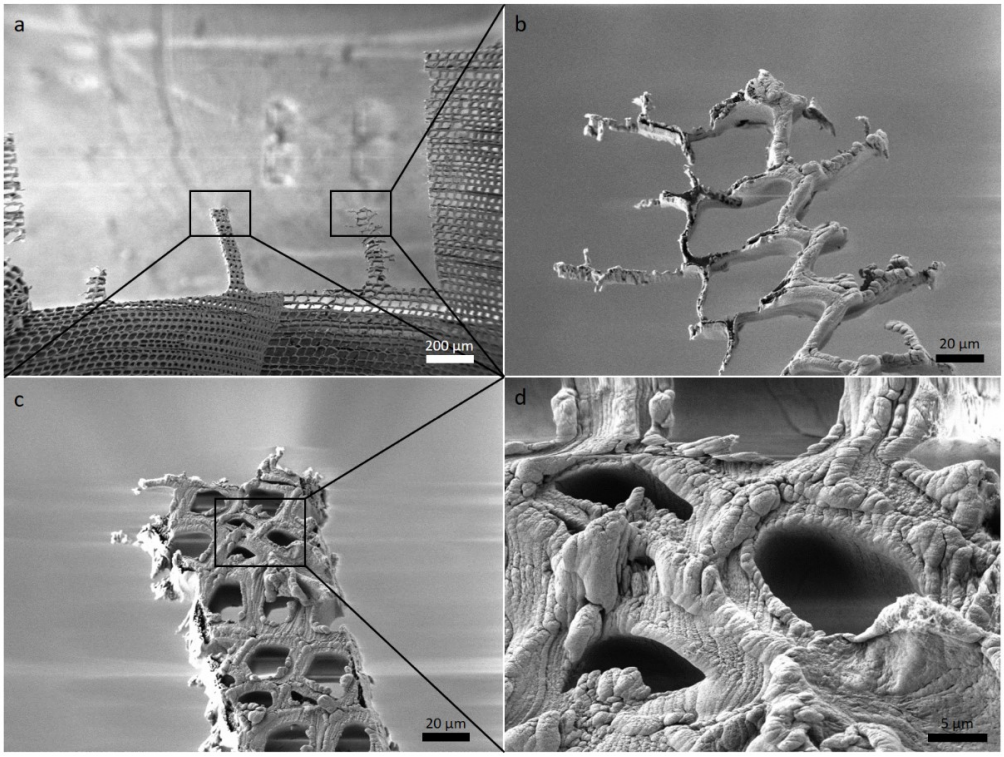

Fig. 40. SEM micrographs of tangential samples prepared by ion milling; (a) overview, (b) larger magnification of an earlywood sample, (c) larger magnification of a latewood sample, (d) surface structure on the latewood sample

4.5.2. Mechanical behaviour

The tensile strength of samples prepared by ion milling was 22 ± 3 MPa on four tests in radial direction. The samples showed brittle behaviour and fracture strains were below 2 %. One sample failed as the piezo tweezers gripped the sample head because of a slight misalignment between sample and tweezers.

4.6. Compressive specimens

4.6.1. Pillar compression with the nanoindenter

Specimens for pillar compression were prepared on tangential and cross sections with 200 µm thickness. The pillars are a remaining cell wall with a more or less trapezoid shape. As already mentioned, it is a matter of chance to get a free-standing pillar as desired. Therefore, only two out of eight samples on the tangential section could be tested. SEM images after indentation revealed a buckled specimen in the shape of a flat triangle (see Fig. 41).

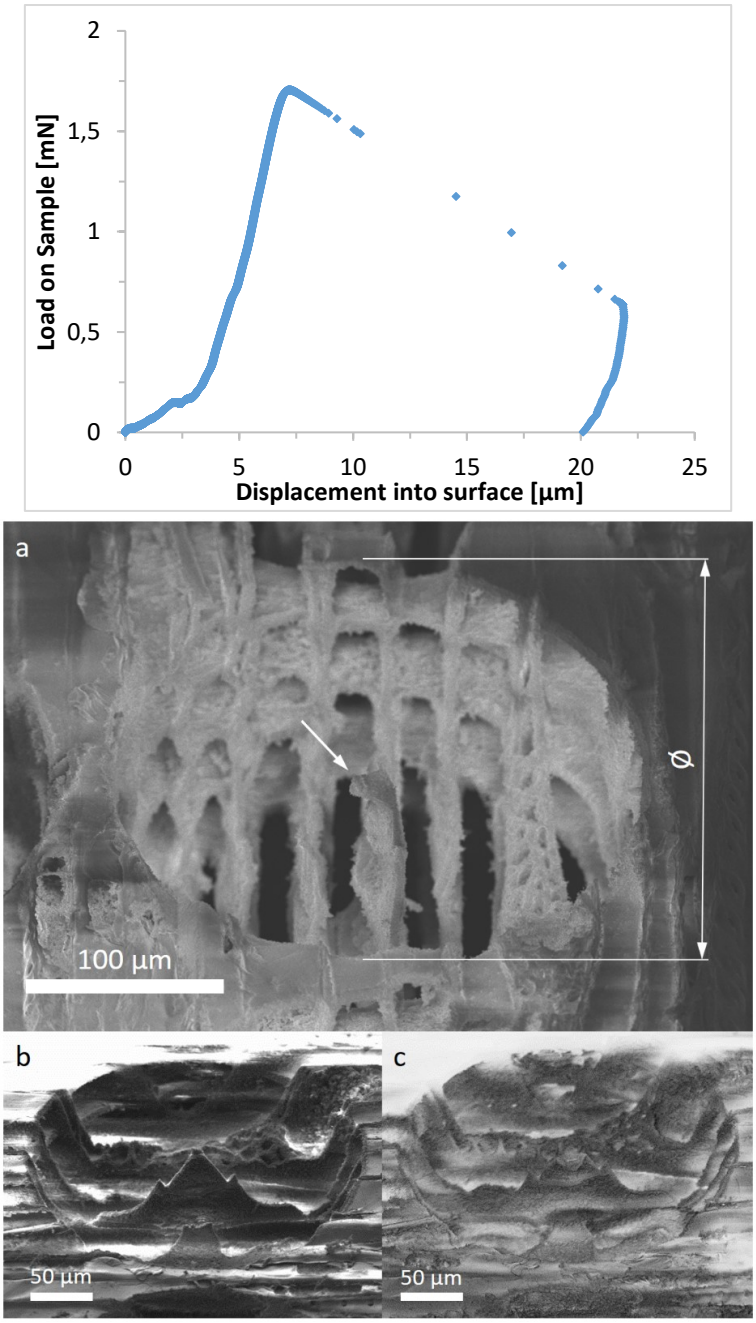

Fig. 41. Load displacement diagram and SEM images of a wood pillar on a tangential section of wood; (a) side view with the diameter of the cut-out cavity indicated and the buckled pillar highlighted by a white arrow; (b) & (c) the same pillar before and after testing in front view

Samples on cross sections could be tested more conveniently. However, due to the taper, which cannot be avoided during laser processing, the pillars had no cylindrical shape. Therefore, the force displacement curve could not be used to calculate the respective stress. One common feature after testing was a flat top surface of the pillars, as shown in Fig. 42.

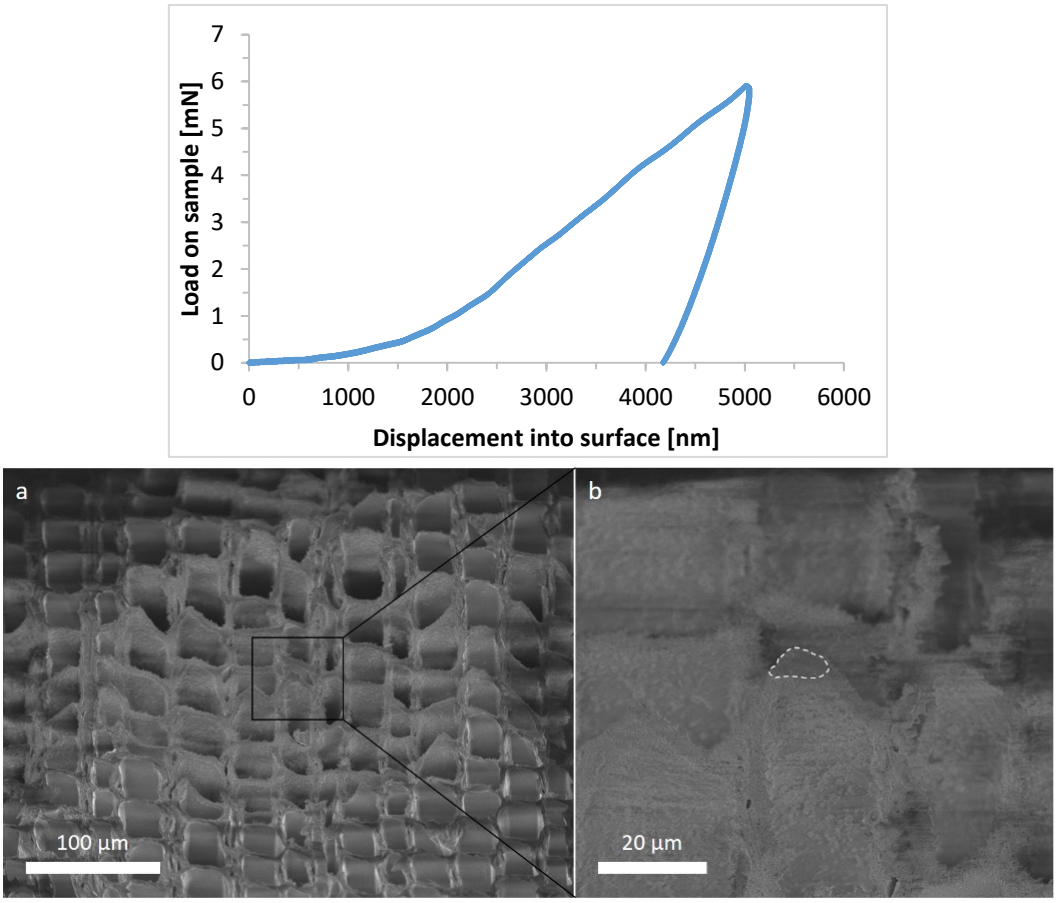

Fig. 42. Load displacement diagram and SEM images of a tested pillar on a cross section of wood; in (b) the flattened top surface is outlined.

4.6.2. Compression experiments with the fibre module

Testing problems related to a non-properly defined sample geometry as seen above were solved by preparing compression samples similar to the previously tested tensile specimens. Rectangular pillars with around 70 µm width were cut into thin sections with a thickness of 60 µm. The aspect ratio was 2:1. The shaft of a high-speed-steel drill was used as an indenter. Displacement was controlled at 1 µm/s deformation speed and the compressive force was recorded. The experiments were observed via a stereomicroscope.

Longitudinal samples

The tested samples in longitudinal direction reached maximum forces between 45 and 207 mN before buckling happened. The force limitation due to the pre-stress of the force measuring tungsten wire was not reached. Fig. 43 shows a typical force displacement diagram. At maximum force the sample buckles and the force drops. During unloading, the sample shows elastic recovery before sample and indenter separate.

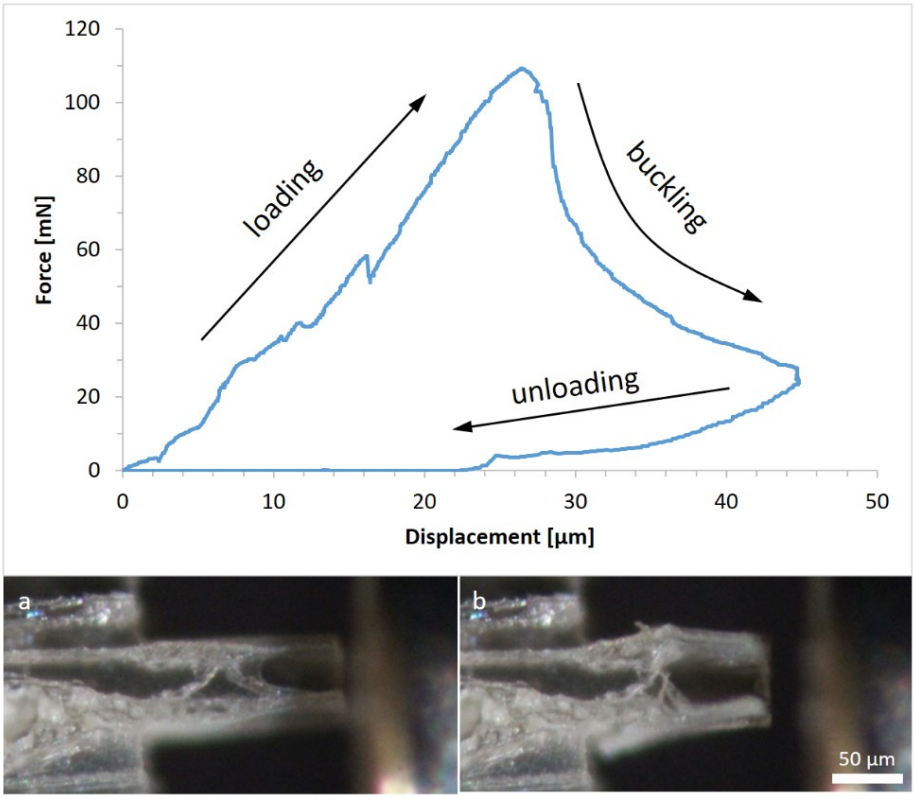

Fig. 43. Typical force displacement diagram of a longitudinal sample in compression; (a) and (b) are optical micrographs of the sample before and after testing.

Samples on cross sections

Compression samples were also cut on cross sections in radial and tangential direction of the trunk. Since the softwood tracheids are cut perpendicular to their axis, the cross section resembles the cellular structure of a honeycomb. Compression tests on these samples confirm the expected cellular behaviour. Fig. 44 shows the force displacement diagrams of four samples tested in radial direction. Every sample has a linear increase in force at the beginning. After the first cell walls collapse the force gets reduced until geometrical densification increases the force again. This results in a more or less even plateau force. All radial samples were located in the earlywood part of the wood section. In tangential direction two out of seven samples were located in the latewood region.

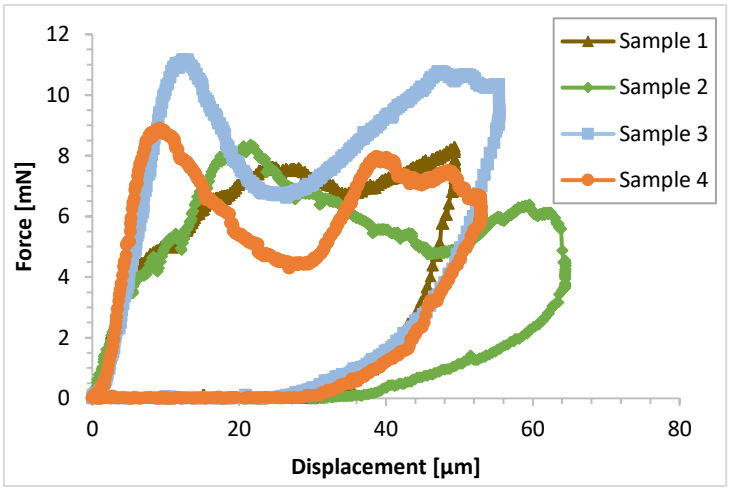

Fig. 44. Force displacement diagrams of four radial compression samples with typical cellular behaviour

The behaviour of cellular materials is strongly dependent on the geometrical density of the honeycomb, as illustrated in Equation 4. Superscript * stands for the cellular material and subscript S for the solid material. Any property P of a cellular material depends on the same property of the solid material building up the cells and the relative density $\frac{\rho^*}{\rho_S}$. The exponent m lies between 1 and 3 and is dependent on the geometry, but not on the material or the dimensions of the cell. [65]

$$P^* \sim P_S \cdot \left(\frac{\rho^*}{\rho_S}\right)^m \qquad (4)$$

For the elastic modulus and the elastic plateau stress of a regular honeycomb the exponent m is 3. Fig. 45 illustrates the density-dependent behaviour of wood. One compression sample in latewood and earlywood is shown respectively. The onsets of the plateau forces, which are 9 and 53 mN respectively, are indicated by dashed lines. Relative densities were estimated as a ratio of cell wall thickness to sample width on a visualized line perpendicular to the loading direction. Relative densities are calculated to be 0.314 and 0.174 for latewood and earlywood respectively. The ratio of plateau forces is the same value as the cubed ratio of densities. This represents elastic buckling of a cellular material.

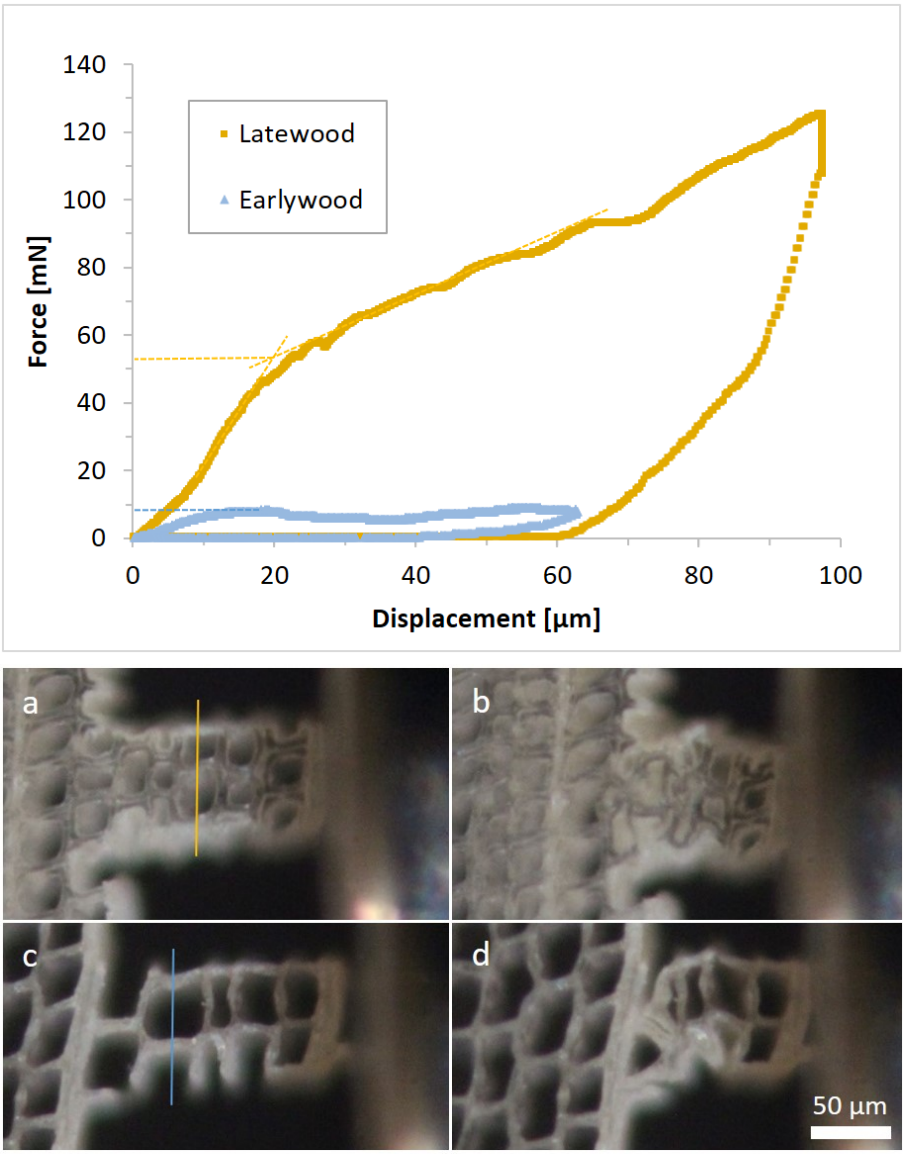

Fig. 45. Force displacement diagram of two tangential compression samples on a cross section; the dashed lines in the diagram indicate the onset forces of cell wall collapses. (a)-(d) are optical micrographs of the tested samples; (a) & (b) show the latewood sample, (c) & (d) the earlywood sample, before testing and at maximum displacement respectively; the lines in (a) and (c) were used for density estimation.

5. Summary

In this work the application of laser ablation with ultrashort pulses was tested on spruce wood. Laser parameters were varied to find optimal parameters for fast cutting with good surface quality. Tensile and compressive specimens were prepared from microtomed thin sections. The samples in different directions were tested in-situ under a stereo microscope with a fibre tensile module.

The received initial material were thin wood sections prepared with a microtome, which is a standard technique for biological materials. The thickness of wood sections can be varied between 50 and 200 µm. The sections were stored in distilled water with sodium azide as conservation agent. For laser processing the sections had to be dried. This was done at ambient conditions between glass sheets. The thin sections were placed on a specimen stub or clamped and fixed on a vice for laser processing.

Laser operation evaporates the irradiated material. The debris is partly carried away by the vacuum pump and partly deposited in the laser chamber similar to a sputter-process. Residues on the f-theta lens can reduce the laser power significantly. To find reproducible parameters, it was found that a clean lens is essential. A slight misalignment of the lenses in the beam expander led to a second ablated hole. After correction of the alignment, a better laser spot was achieved.

Before use, the fibre tensile module had to be calibrated for correct detection of force and displacement. The force measurement is based on an oscillating tungsten wire, which can withstand a maximum force of 1 N. Since the wood sections are clamped on the same device as for testing on the fibre tensile setup, handling of samples is easy and efficient. Sample heads could be gripped by piezo actuated tweezers or glued with conductive carbon cement on a silicon piece.

Tensile samples tested in longitudinal direction exhibit in most cases intrawall failure and in one case transwall failure. The fracture surface is serrated with the crack path along the microfibril angle and across microfibrils alternately and also along interfaces of wood rays. On cross sections two failure modes for tensile tests are observed, cell wall rupture and fibre debonding. Also in tangential samples cell wall rupture was the dominant failure mode, which could be explained by the sample size and the brick wall structure of wood.

For the calculation of stress values, the cell wall dimensions have to be measured. Since the fracture surface is not flat, fractured cross sections are estimated by measuring the cell wall thickness from optical micrographs. The error margin adds up to 14 %.

Two samples were exposed to an electron beam at 1 kV acceleration voltage. Three other samples on the same thin section had already been tested for comparison. The failure mode in both electron-irradiated samples was fibre debonding. Tensile strength was only a fifth compared to the same failure mode in unexposed samples.

Compressive samples were tested with the same setup as for tensile specimens. Samples in longitudinal direction buckled. The samples on cross sections showed the typical cellular behaviour of a honeycomb under compressive loading. After linear elastic response, cell walls collapse and the force remains at a plateau until geometrical densification leads to an increase in force. Furthermore, the dependency on density was demonstrated.

Alternative preparation techniques for wood samples in micrometre dimensions are limited. Single wood fibres can be mechanically isolated, but the mechanical response of interacting fibres is lost. Microtoming reduces only one dimension of a sample. Another machining technique in this size range, namely electrical discharge machining, is limited to conducting materials and therefore not suitable for wood. Micro-milling is a precise machining technique, but is expected to be too rough for a good surface quality and unaffected specimens. The FIB has been used for preparation of pillars on the cell wall, but with larger sample dimensions, the operation time would be days. An already tried preparation technique for non-conductive foils is ion milling with a copper mask. This alternative route provided wood samples after several hours of exposure to the ion beam in vacuum. However, this exposure has a negative effect on the samples. A colour change from slight brown to even black is apparent to the naked eye. Mechanical values are low and the samples showed brittle behaviour.

This work has shown that laser processing is a fast and efficient technique for the preparation of wood samples for micromechanical testing. All dimensions can be set in the micrometre range. The laser processing leads to a grainy surface at incised regions but has otherwise no effect on the material. This surface layer is only one micrometre thick, which is negligibly small compared to the thickness of the samples investigated in this study. Furthermore, this preparation technique is not limited to wood but can be applied to foils of any material.

List of symbols and abbreviations

fs	Femtoseconds
FIB	Focused ion beam workstation
SEM	Scanning electron microscope
S_1, S_2, S_3	Layers of the secondary cell wall
MFA	Microfibril angle
Nd:YAG	Neodymium doped Yttrium Aluminium garnet
Yb:YAG	Ytterbium doped Yttrium Aluminium garnet
ps	Picoseconds
h	Planck constant
v	Frequency
E_g	Bandgap energy
E_{pulse}	Pulse energy
P	Average laser power
f	Pulse repetition rate
$E_{fluence}$	Laser fluence
A_f	Focal area of the laser spot
CW	Continuous wave
α	Clearance angle
β	Knife angle
γ	Declination angle
WD	Working distance
k	Linearity factor
CCC	Conductive carbon cement
D	Divisor
v_s	Scan speed
s	Separation of laser spots
LD	Lens distance
λ	Laser wavelength
L	Layer
S	Scan repetition rate
σ	Stress
CML	Compound middle lamella
P^*	Property of the cellular material
P_S	Property of the solid material
$\frac{\rho^*}{\rho_S}$	Relative density of the cellular material
m	Geometry dependent exponent

List of figures

Fig. 1. Cross section through a fir tree (adapted from Dinwoodie, 2000) [18] 3
Fig. 2. Three-dimensional model of softwood structure (adaptation from Mägdefrau, 1951) [19]..... 4
Fig. 3. Three-dimensional model of hardwood structure (adaptation from Mägdefrau, 1951) [19] 5
Fig. 4. Schematic structure of the cell wall of a softwood tracheid [18]..... 6
Fig. 5. Scheme of Chirped Pulse Amplification [25] 8
Fig. 6. Electron excitation by single- and multi-photon absorption [17]..... 9
Fig. 7. Schematic knife geometry of a microtome; left: side view with clearance angle α and knife angle β, right: top view with declination angle γ 11
Fig. 8. Photograph of the laser system giving an overview with main components labelled (courtesy of M. Pfeifenberger, Erich Schmid Institute, 2016) 12
Fig. 9. Scheme of the beam expander for adjusting the WD (courtesy of M. Pfeifenberger, Erich Schmid Institute, 2016) 13
Fig. 10. Principle setup of the laser system (courtesy of M. Pfeifenberger, Erich Schmid Institute, 2016)..... 14
Fig. 11. Schematics of the ion gun and sample stage (left) and the free-standing copper specimen used as a mask (right) [43, 44]..... 15
Fig. 12. Schematic diagram of the G200 Nano Indenter [48]..... 16
Fig. 13. Photograph of the fibre tensile module with the following components: (1) Base, (2) Main stage, (3) Transformer, (4) Specimen stage, (5) Specimen clamp, (6) Piezo tweezers, (7) Flexible stage, (8) Motor, (9) Magnetic gap, (10) Controller connector [49]..... 17
Fig. 14. Exemplary illustration of a sledge microtome from company C. Reichert Wien [50] 19
Fig. 15. Optical micrograph with a set of lines cut with 10 passes, a divisor of 50 and different laser power, 159 mW (left) to 319 mW (right); arrows indicate the position of the vertical lines. . 22
Fig. 16. Optical micrograph illustrating the ablation kerf at maximum power of 638mW, 10 passes, divisor set to 50 23
Fig. 17. Optical micrograph illustrating the heat accumulation at divisor values of 1 and 10, which lead to the destruction of the material; power set to 287 mW and 10 passes scanned 24
Fig. 18. Optical micrograph of lines with 100 layers (top) and 10 layers (bottom) cut at 287 mW power and a divisor of 50 25
Fig. 19. Optical micrograph with variation of the lens distance (LD) of the beam expander, 287 mW laser power, 100 passes, divisor 100..... 26
Fig. 20. Optical micrograph of holes cut with different LD, power was 319 mW, divisor set to 250, ablation time of 20 s; a second ablated hole at every position is visible. 26
Fig. 21. Geometry for laser cutting of tensile specimens; the shaded region indicates the remaining material after cutting..... 28
Fig. 22. Optical micrographs of tensile specimens on a cross section (a) and a tangential section of wood (b) 28
Fig. 23. Optical micrograph of the Cu-mask with already etched wood underneath..... 29
Fig. 24. Optical micrograph of an array of six tensile samples after ion irradiation; the colour change at the edges is apparent to the naked eye. 30
Fig. 25. Cutting geometry for laser processing of compression samples; shaded regions indicate the remaining material. 31
Fig. 26. Optical micrograph of the indenter in the proximity of tested compression samples 32

Fig. 27. Schematics of the three different failure types in longitudinal direction according to Côté and Hanna [3] 33
Fig. 28. Simplified morphological model of a softwood cross section and crack propagation for radial and tangential loading [62] 34
Fig. 29. Typical force displacement diagram of a longitudinal sample, the optical micrographs below are taken at the marked points a-c; (a) specimen before any displacement is applied, the area of an intersecting wood ray is indicated by the dashed line; (b) the onset of a crack is indicated by an arrow; (c) fractured specimen 35
Fig. 30. SEM micrograph of a fracture surface section of a longitudinal sample viewed in loading direction; the different cell wall layers are indicated, the compound middle lamella (CML) consists of the primary wall and the middle lamella; crack propagation in the S_2 layer was along the MFA and failed microfibril packages alternately. 36
Fig. 31. Optical micrograph of a fractured radial sample with microfibrils still connecting the two fragments 37
Fig. 32. SEM micrograph of a fractured sample loaded in radial direction; (a) rupture of the cell walls, (b) still intact S_3 layer at the lumen area, (c) laser-processed surface, (d) delamination of the middle lamella 37
Fig. 33. Force displacement diagram for a tensile test in tangential direction; the optical micrographs below show the sample corresponding to loading stages a-d; (a) unloaded specimen; white arrow in (b) indicates cell wall rupture; white arrow in (c) indicates fibre debonding; (d) rupture of the remaining connection 38
Fig. 34. Optical micrograph of a fracture surface of a radial sample viewed in loading direction; the dashed line indicates the overall dimensions of the sample, whereas the highlighted areas mark the fractured cell walls determining the tensile strength. 40
Fig. 35. Optical micrographs of a radial sample exposed to the electron beam in the SEM; (a) unloaded specimen; (b) failure through fibre debonding 42
Fig. 36. Comparison of tensile strength of fibre debonding between samples, exposed and unexposed to electrons with 1 kV in the SEM 42
Fig. 37. SEM micrographs of the surface of thin sections after microtome cutting; (a) earlywood and (b) latewood 43
Fig. 38. SEM micrographs of a fs-laser processed surface; (a) next to the laser kerf the intact S_3 layer with pits is visible, (b) larger magnification of the laser incised surface 44
Fig. 39. SEM images of radial samples prepared by ion milling; (a) an untested sample, (b) Sample head glued to a silicon piece with CCC, (c) detail of (a) showing loosely connected wood cells, (d) detail of (b) showing maybe melted wood components on the surface in a region shadowed by the copper mask during ion irradiation 44
Fig. 40. SEM micrographs of tangential samples prepared by ion milling; (a) overview, (b) larger magnification of an earlywood sample, (c) larger magnification of a latewood sample, (d) surface structure on the latewood sample 45
Fig. 41. Load displacement diagram and SEM images of a wood pillar on a tangential section of wood; (a) side view with the diameter of the cut-out cavity indicated and the buckled pillar highlighted by a white arrow; (b) & (c) the same pillar before and after testing in front view 46
Fig. 42. Load displacement diagram and SEM images of a tested pillar on a cross section of wood; in (b) the flattened top surface is outlined. 47
Fig. 43. Typical force displacement diagram of a longitudinal sample in compression; (a) and (b) are optical micrographs of the sample before and after testing. 48

Fig. 44. Force displacement diagrams of four radial compression samples with typical cellular behaviour..... 49
Fig. 45. Force displacement diagram of two tangential compression samples on a cross section; the dashed lines in the diagram indicate the onset forces of cell wall collapses. (a)-(d) are optical micrographs of the tested samples; (a) & (b) show the latewood sample, (c) & (d) the earlywood sample, before testing and at maximum displacement respectively; the lines in (a) and (c) were used for density estimation..... 50

List of tables

Table 1: Separation of consecutive laser pulses at different divisor values with v_s = 1 mm/s and f = 50 kHz ……24
Table 2: Final parameter set for preparation of tensile specimen ……27
Table 3: Tensile strength of cell walls in transverse direction on different microtomed cross sections ……41

References

[1] U. G. K. Wegst, H. Bai, E. Saiz, A. P. Tomsia, R. O. Ritchie, “Bioinspired structural materials,” *Nat. Mater.*, vol. 14, pp. 23–36, 2015.

[2] M. Eder, O. Arnould, J. W. C. Dunlop, J. Hornatowska, and L. Salmén, “Experimental micromechanical characterisation of wood cell walls,” *Wood Sci. Technol.*, vol. 47, pp. 163–182, 2013.

[3] G. Kifetew, F. Thuvander, L. Berglund, and H. Lindberg, “The effect of drying on wood fracture surfaces from specimens loaded in wet condition,” *Wood Sci. Technol.*, vol. 32, pp. 83–94, 1998.

[4] L. Mott, S. Shaler, and L. Groom, “A Technique to Measure Strain Distributions in Single Wood Pulp Fibers,” *Wood Fiber Sci.*, vol. 28, pp. 429–437, 1996.

[5] I. Burgert, K. Frühmann, J. Keckes, P. Fratzl, and S. E. Stanzl-Tschegg, “Microtensile Testing of Wood Fibers Combined with Video Extensometry for Efficient Strain Detection,” *Holzforschung*, vol. 57, pp. 661–664, 2003.

[6] Y. Yu, Z. Jiang, B. Fei, G. Wang, and H. Wang, “An improved microtensile technique for mechanical characterization of short plant fibers: A case study on bamboo fibers,” *J. Mater. Sci.*, vol. 46, pp. 739–746, 2011.

[7] S. Orso, U. G. K. Wegst, and E. Arzt, “The elastic modulus of spruce wood cell wall material measured by an in situ bending technique,” *J. Mater. Sci.*, vol. 41, pp. 5122–5126, 2006.

[8] R. B. Adusumalli, R. Raghavan, R. Ghisleni, T. Zimmermann, and J. Michler, “Deformation and failure mechanism of secondary cell wall in Spruce late wood,” *Appl. Phys. A Mater. Sci. Process.*, vol. 100, pp. 447–452, 2010.

[9] R. Raghavan, R. B. Adusumalli, G. Buerki, S. Hansen, T. Zimmermann, and J. Michler, “Deformation of the compound middle lamella in spruce latewood by micro-pillar compression of double cell walls,” *J. Mater. Sci.*, vol. 47, pp. 6125–6130, 2012.

[10] X. Zhang, Q. Zhao, S. Wang, R. Trejo, E. Lara-Curzio, and G. Du, “Characterizing strength and fracture of wood cell wall through uniaxial micro-compression test,” *Compos. Part A Appl. Sci. Manuf.*, vol. 41, pp. 632–638, 2010.

[11] R. Wimmer, B. N. Lucas, T. Y. Tsui, and W. C. Oliver, “Longitudinal hardness and Young’s modulus of spruce tracheid secondary walls using nanoindentation technique,” *Wood Sci. Technol.*, vol. 31, pp. 131–141, 1997.

[12] W. Gindl, H. S. Gupta, T. Schöberl, H. C. Lichtenegger, and P. Fratzl, “Mechanical properties of spruce wood cell walls by nanoindentation,” *Appl. Phys. A Mater. Sci. Process.*, vol. 79, pp. 2069–2073, 2004.

[13] A. Jäger, K. Hofstetter, C. Buksnowitz, W. Gindl-Altmutter, and J. Konnerth, “Identification of stiffness tensor components of wood cell walls by means of nanoindentation,” *Compos. Part A Appl. Sci. Manuf.*, vol. 42, pp. 2101–2109, 2011.

[14] M. P. Echlin, N. S. Husseini, J. A. Nees, and T. M. Pollock, “A new femtosecond laser-based tomography technique for multiphase materials,” *Adv. Mater.*, vol. 23, pp. 2339–2342, 2011.

[15] D. Kiener, C. Motz, M. Rester, M. Jenko, and G. Dehm, “FIB damage of Cu and possible consequences for miniaturized mechanical tests,” *Mater. Sci. Eng. A*, vol. 459, pp. 262–272, 2007.

[16] Q. Feng, Y. N. Picard, H. Liu, S. M. Yalisove, G. Mourou, and T. M. Pollock, “Femtosecond laser micromachining of a single-crystal superalloy,” *Scr. Mater.*, vol. 53, pp. 511–516, 2005.

[17] K. Sugioka and Y. Cheng, Eds., *Ultrafast Laser Processing*. Pan Stanford Publishing, 2013.

[18] J. M. Dinwoodie, *Timber: It’s nature and behaviour*, 2nd Editio. London: E & FN Spon, 2000.

[19] H. C. Lichtenegger, “The composite architecture of the wood cell wall,” doctoral thesis, University of Vienna, 1991.

[20] S. Mishra and V. Yadava, “Laser Beam MicroMachining (LBMM) - A review,” *Opt. Lasers Eng.*, vol. 73, pp. 89–122, 2015.

[21] S. Küper and M. Stuke, “Femtosecond uv excimer laser ablation,” *Appl. Phys. B Photophysics Laser Chem.*, vol. 44, pp. 199–204, 1987.

[22] R. Srinivasan, E. Sutcliffe, and B. Braren, “Ablation and etching of polymethylmethacrylate by very short (160 fs) ultraviolet (308 nm) laser pulses,” *Appl. Phys. Lett.*, vol. 51, pp. 1285–1287, 1987.

[23] M. C. Gower, “Industrial applications of laser micromachining.,” *Opt. Express*, vol. 7, pp. 56–67, 2000.

[24] F. Korte, J. Serbin, J. Koch, A. Egbert, C. Fallnich, A. Ostendorf, and B. N. Chichkov, “Towards nanostructuring with femtosecond laser pulses,” *Appl. Phys. A Mater. Sci. Process.*, vol. 77, pp. 229–235, 2003.

[25] M. Castillejo, P. M. Ossi, and L. Zhigilei, Eds., *Lasers in Material Science*. Springer, 2014.

[26] M. K. Reed, M. K. Steiner-Shepard, and D. K. Negus, “Widely tunable femtosecond optical parametric amplifier at 250 kHz with a Ti:sapphire regenerative amplifier.,” *Opt. Lett.*, vol. 19, pp. 1855–1857, 1994.

[27] P. Lacovara, H. K. Choi, C. A. Wang, R. L. Aggarwal, and T. Y. Fan, “Room-temperature diode-pumped Yb:YAG laser.,” *Opt. Lett.*, vol. 16, pp. 1089–1091, 1991.

[28] D. Strickland and G. Mourou, “Compression of Amplified Chirped Optical Pulses *,” *Opt. Commun.*, vol. 56, pp. 219–221, 1985.

[29] X. Liu, D. Du, and G. Mourou, “Laser ablation and micromachining with ultrashort laser pulses,” *IEEE J. Quantum Electron.*, vol. 33, pp. 1706–1716, 1997.

[30] L. Jiang and H.-L. Tsai, “Improved Two-Temperature Model and Its Application in Ultrashort Laser Heating of Metal Films,” *J. Heat Transfer*, vol. 127, pp. 1167–1173, 2005.

[31] C. Leone, V. Lopresto, and I. De Iorio, “Wood engraving by Q-switched diode-pumped frequency-doubled Nd:YAG green laser,” *Opt. Lasers Eng.*, vol. 47, pp. 161–168, 2009.

[32] M. N. Islam, K. Ando, H. Yamauchi, Y. Kobayashi, and N. Hattori, “Comparative study between full cell and passive impregnation method of wood preservation for laser incised Douglas fir lumber,” *Wood Sci. Technol.*, vol. 42, pp. 343–350, 2008.

[33] J. C. Hernandez-Castaneda, H. K. Sezer, and L. Li, “Statistical analysis of ytterbium-doped fibre laser cutting of dry pine wood,” *Proc. Inst. Mech. Eng. Part B-Journal Eng. Manuf.*, vol. 223, pp. 775–789, 2009.

[34] M. Panzner, G. Wiedemann, K. Henneberg, R. Fischer, T. Wittke, and R. Dietsch, “Experimental investigation of the laser ablation process on wood surfaces,” *Appl. Surf. Sci.*, vol. 127–129, pp. 787–792, 1998.

[35] Y. Wang, K. Ando, and N. Hattori, “Changes in the anatomy of surface and liquid uptake of wood after laser incising,” *Wood Sci. Technol.*, vol. 47, pp. 447–455, 2013.

[36] J. Seltman, “Freilegen der Holzstruktur durch UV-Bestrahlung,” *Holz als Roh- und Werkst.*, vol. 53, pp. 225–228, 1995.

[37] S. Fukuta, M. Nomura, T. Ikeda, M. Yoshizawa, M. Yamasaki, and Y. Sasaki, “UV laser machining of wood,” *Eur. J. Wood Wood Prod.*, vol. 74, pp. 261–267, 2016.

[38] N. Naderi, S. Legacéy, and S. L. Chin, “Preliminary investigations of ultrafast intense laser wood processing,” *For. Prod. J.*, vol. 49, pp. 72–76, 1999.

[39] E. Baubeau, R. Le Harzic, C. Jonin, E. Audouard, S. Mottin, M. Courbon, and P. Laporte, “Micromachining with high repetition rate femtosecond laser sources,” *1st Int. Symp. Laser Precis. Microfabr. Proc. SPIE*, vol. 4088, pp. 48–50, 2000.

[40] F. Théberge, S. Petit, A. Iwasaki, M. R. Kasaai, and S. L. Chin, “Ultrafast intense laser ‘explosion’ of hardwood,” *Appl. Surf. Sci.*, vol. 191, pp. 328–333, 2002.

[41] B. Bracegirdle, *A history of microtechnique: the evolution of the microtome and the development of tissue preparation*. London: Heinemann Educational Books, 1978.

[42] M. P. Echlin, M. Straw, S. Randolph, J. Filevich, and T. M. Pollock, “The TriBeam system: Femtosecond laser ablation in situ SEM,” *Mater. Charact.*, vol. 100, pp. 1–12, 2015.

[43] Hitachi High Technologies America Inc. *E-3500 Ion Milling System manual*

[44] M. Smolka, C. Motz, T. Detzel, W. Robl, T. Griesser, A. Wimmer, and G. Dehm, “Novel temperature dependent tensile test of freestanding copper thin film structures,” *Rev. Sci. Instrum.*, vol. 83, 2012.

[45] M. D. Uchic, D. M. Dimiduk, J. N. Florando, and W. D. Nix, “Sample Dimensions Influence Strength and Crystal Plasticity,” *Science*, vol. 305, pp. 986–989, 2004.

[46] M. F. Doerner and W. D. Nix, “A method for interpreting the data from depth-sensing indentation instruments,” *J. Mater. Res.*, vol. 1, pp. 601–609, 1986.

[47] C. Oliver and M. Pharr, “An improved technique for determining hardness and elastic modulus using load and displacement sensing indentation experiments,” *J. Mater. Res.*, vol. 7, pp. 1564–1583, 1992.

[48] “http://www.keysight.com/en/pd-1675520-pn-U9820A/agilent-nano-indenter-g200,” August 2016.

[49] B. Yang, C. Motz, W. Grosinger, W. Kammrath, and G. Dehm, “Tensile behaviour of micro-sized copper wires studied using a novel fibre tensile module,” *Int. J. Mat. Res.*, vol. 99, pp. 716–724, 2008.

[50] “http://www.klaus-henkel.de/cut-mikrotom.html,” August 2016.

[51] L. Groom, L. Mott, and S. Shaler, “Mechanical Properties of Individual Southern Pine Fibers Part I. Determination and Variability of Stress-Strain Curves with Respect to Tree Height and Juvenility,” *WOOD FIBER Sci.*, vol. 34, pp. 14–27, 2002.

[52] I. Burgert, N. Gierlinger, and T. Zimmermann, “Properties of chemically and mechanically isolated fibres of spruce (Picea abies [L.] Karst.). Part 1: Structural and chemical characterisation,” *Holzforschung*, vol. 59, pp. 240–246, 2005.

[53] P. Hoffmeyer and R. B. Hanna, “Electron beam damage during testing of wood in the SEM,” *Wood Sci. Technol.*, vol. 23, pp. 211–214, 1989.

[54] J. Bodner, G. Grüll, and M. G. Schlag, “In-situ Fracturing of Wood in the Scanning Electron Microscope,” *Holzforschung*, vol. 50, pp. 487–490, 1996.

[55] C. C. Gerhards, “Effect of moisture content and temperature on the mechanical properties of wood: an analysis of immediate effects,” *Wood Fiber Sci.*, vol. 14, pp. 4–36, 1982.

[56] L. P. Futó, “Qualitative und quantitative Ermittlung der Mikrozugeigenschaften von Holz,” *Holz als Roh- und Werkst. Eur. J. Wood Wood Ind.*, vol. 27, pp. 192–201, 1969.

[57] M. Sippola and K. Frühmann, “In situ Longitudinal Tensile Tests of Pine Wood in an Environmental Scanning Electron Microscope,” *Holzforschung*, vol. 56, pp. 669–675, 2002.

[58] J. Bodner, M. G. Schlag, and G. Grüll, “Fracture initiation and progress in wood specimens stressed in tension - Part I. Clear wood specimens stressed parallel to the grain,” *Holzforschung*, vol. 51, pp. 479–484, 1997.

[59] L. Mott, S. M. Shaler, L. H. Groom, and D. Liang, “The tensile testing of individual wood fibers using environmental scanning electron microscopy and video image analysis,” *Tappi J.*, vol. 78, pp. 143–148, 1995.

[60] M. Eder, S. Stanzl-Tschegg, and I. Burgert, “The fracture behaviour of single wood fibres is governed by geometrical constraints: In situ ESEM studies on three fibre types,” *Wood Sci. Technol.*, vol. 42, pp. 679–689, 2008.

[61] W. A. Côté and R. B. Hanna, “Ultrastructural characteristics of wood fracture surfaces,” *Wood Fiber Sci,* vol. 15, pp. 135–163, 1983.

[62] G. Dill-Langer, S. Lütze, and S. Aicher, “Microfracture in wood monitored by confocal laser scanning microscopy,” *Wood Sci. Technol.*, vol. 36, pp. 487–499, 2002.

[63] M. Eder, K. Jungnikl, and I. Burgert, “A close-up view of wood structure and properties across a growth ring of Norway spruce (Picea abies [L] Karst.),” *Trees - Struct. Funct.*, vol. 23, pp. 79–84, 2009.

[64] E. N. Tokareva, P. Fardim, A. V. Pranovich, H. P. Fagerholm, G. Daniel, and B. Holmbom, “Imaging of wood tissue by ToF-SIMS: Critical evaluation and development of sample preparation techniques,” *Appl. Surf. Sci.*, vol. 253, pp. 7569–7577, 2007.

[65] L. J. Gibson, M. F. Ashby, G. S. Schajer, and C. I. Robertson, “The mechanics of two-dimensional cellular materials,” *Proc. R. Soc. London A*, vol. 382, pp. 25–42, 1982.